

# First Light And Reionisation Epoch Simulations (FLARES) XX: Comparing semi-analytic models at high-redshift

Louise T. C. Seeyave<sup>1\*</sup>, Carlton M. Baugh<sup>2</sup>, Ángel Chandro-Gómez<sup>3</sup>, Claudia del P. Lagos<sup>3</sup>, Robert M. Yates<sup>4</sup>, L. Y. Aaron Yung<sup>5</sup>, Rachel S. Somerville<sup>6</sup>, Stephen M. Wilkins<sup>1,7</sup>, Christopher C. Lovell<sup>8,9</sup>, William J. Roper<sup>1</sup>, Aswin P. Vijayan<sup>1</sup>, Cedric G. Lacey<sup>2</sup>, Chris Power<sup>3</sup>, Shihong Liao<sup>10</sup>, Maxwell G. A. Maltz<sup>1</sup>, Jack C. Turner<sup>1</sup>

<sup>1</sup>*Astronomy Centre, University of Sussex, Falmer, Brighton BN1 9QH, UK*

<sup>2</sup>*Institute for Computational Cosmology, Department of Physics, Science Laboratories, South Road, Durham, DH1 3LE, UK*

<sup>3</sup>*International Centre for Radio Astronomy Research, The University of Western Australia, M468, 35 Stirling Highway, Crawley, WA 6009, Australia*

<sup>4</sup>*Centre for Astrophysics Research, University of Hertfordshire, Hatfield, AL10 9AB, UK*

<sup>5</sup>*Space Telescope Science Institute, 3700 San Martin Dr., Baltimore, MD 21218, USA*

<sup>6</sup>*Center for Computational Astrophysics, Flatiron Institute, 162 5th Avenue, New York, NY 10010, USA*

<sup>7</sup>*Institute of Space Sciences and Astronomy, University of Malta, Msida MSD 2080, Malta*

<sup>8</sup>*Kavli Institute for Cosmology, Madingley Road, Cambridge CB3 0HA, UK*

<sup>9</sup>*Institute of Astronomy, Madingley Road, Cambridge CB3 0HA, UK*

<sup>10</sup>*Key Laboratory for Computational Astrophysics, National Astronomical Observatories, Chinese Academy of Sciences, Beijing 100101, China*

Accepted XXX. Received YYY; in original form ZZZ

## ABSTRACT

We explore how the choice of galaxy formation model affects the predicted properties of high-redshift galaxies. Using the FLARES zoom resimulation strategy, we compare the EAGLE hydrodynamics model and the GALFORM, L-GALAXIES, SC-SAM and SHARK semi-analytic models (SAMs) at  $5 \leq z \leq 12$ . The first part of our analysis examines the stellar mass functions, stellar-to-halo mass relations, star formation rates, and supermassive black hole (SMBH) properties predicted by the different models. Comparisons are made with observations, where relevant. We find general agreement between the range of predicted and observed stellar mass functions. The model predictions differ considerably when it comes to SMBH properties, with GALFORM and SHARK predicting between 1.5 – 3 dex more massive SMBHs ( $M_{\text{BH}} > 10^6 M_{\odot}$ ) than L-GALAXIES and SC-SAM, depending on redshift. The second half of our analysis focuses on passive galaxies. We show that in L-GALAXIES and SC-SAM, environmental quenching of satellites is the prevalent quenching mechanism, with active galactic nuclei (AGN) feedback having little effect at the redshifts probed. On the other hand,  $\sim 40\%$  of passive galaxies predicted by GALFORM and SHARK are quenched by AGN feedback at  $z = 5$ . The SAMs are an interesting contrast to the EAGLE model, in which AGN feedback is essential for the formation of passive galaxies, in both satellites and centrals, even at high redshift.

**Key words:** galaxies: high-redshift – galaxies: evolution – galaxies: abundances

## 1 INTRODUCTION

Galaxy formation and evolution is a rich interplay of numerous physical processes. In hierarchical structure formation, a feature of the widely-used  $\Lambda$ CDM cosmological model, gravitationally-bound dark matter halos grow through repeated mergers. Baryonic matter traces the distribution of dark matter, with gas accreting onto dark matter halos and cooling to form stars. Over time, these clusters of gas and stars merge to form galaxies. Key baryonic processes in galaxies include: the aforementioned formation of stars from cold gas, stellar feedback heating up the interstellar medium (ISM) and enriching it with metals, the formation of black holes and their subsequent growth through accretion of matter, and feedback from active galactic nuclei

(AGN) in the form of radiation and jets. Galaxies are also affected by their environment, for example, through tidal interactions or mergers with other galaxies (Benson 2010; Somerville & Davé 2015).

The picture of how galaxies form and evolve is continually developing. In the last few years, observations by the *James Webb Space Telescope* (JWST, Gardner et al. 2006) have opened up new debate around our understanding of high-redshift ( $z > 5$ ) galaxies. Much emphasis has been placed on the large numbers of UV-luminous galaxies observed at  $z > 10$  (Castellano et al. 2023; Finkelstein et al. 2023; Leung et al. 2023; Adams et al. 2024; Finkelstein et al. 2024; Robertson et al. 2024; Whittler et al. 2025), the abundance of passive galaxies measured at  $z = 4 - 5$  (Alberts et al. 2024; Russell et al. 2024; Weibel et al. 2024a; Xiao et al. 2024; Baker et al. 2025; Zhang et al. 2025), as well as the populations of AGN discovered at  $z = 5 - 8$  (Harikane et al. 2023; Greene et al. 2024; Matthee et al. 2024). Some findings, particularly those at higher redshifts, are in excess of a num-

\* E-mail: L.Seeyave@sussex.ac.uk.

Note that the order of the author list is explained in the acknowledgements.

ber of theoretical predictions (Lovell et al. 2023a; Adams et al. 2024; Weibel et al. 2024a). However, physical properties estimated from observations are often subject to large uncertainties (Suess et al. 2022; Desprez et al. 2024; Trussler et al. 2024; Narayanan et al. 2024). In addition, theoretical studies have suggested that the tension between observed and predicted UV luminosity functions (UVLFs) can be reduced with reasonable adaptations to the physics modelling, for example, by increasing the star formation efficiency (Lu et al. 2025; Somerville et al. 2025) or invoking bursty star formation (Sun et al. 2023; Gelli et al. 2024).

Passive galaxies, also known as ‘quiescent’ or ‘quenched’ galaxies, are those in which star formation has ceased. This can occur through internal channels, such as feedback events that heat and expel cold gas, leaving little to form stars. In low-mass galaxies, stellar feedback is sufficient to drive such a process (Merlin et al. 2012), while in high-mass galaxies, AGN feedback is thought to be required for gas to escape the deeper potential wells (Di Matteo et al. 2005; Croton et al. 2006; Somerville et al. 2008). Environmental processes can also drive passivity. Satellites may be ‘starved’ of cold gas (Feldmann & Mayer 2015; Trussler et al. 2020), or undergo ram pressure stripping as they travel through the intracluster medium (ICM; Simpson et al. 2018; Xu et al. 2025). Since dense galaxy clusters do not yet exist at  $z > 2$  (Overzier 2016), environmental processes are expected to play less of a role at high redshifts. The number density of passive galaxies in the early universe may thus offer useful information about the aforementioned internal feedback channels.

There are two main approaches to modelling the physics involved in galaxy formation and evolution – semi-analytic models (SAMs) and numerical hydrodynamic simulations. In SAMs, galaxies are modelled analytically atop the merger histories of dark matter halos. These merger histories are encapsulated in merger trees, which can be obtained from dark matter-only (DMO) N-body simulations (Behroozi et al. 2013b; Elahi et al. 2019; Roper et al. 2020) or Extended Press-Schechter (EPS) methods (Somerville & Kolatt 1999; Somerville et al. 2008). Physical processes in SAMs are described by equations that manipulate flows of baryonic material to and from different ‘reservoirs’, typically representing stars, black holes, interstellar cold gas, circumgalactic hot gas and intracluster/intergalactic hot gas. Stellar and cold gas reservoirs may be split into bulge and disk components, or finer annuli (Kauffmann 1996; Baugh et al. 1996; Fu et al. 2010; Porter et al. 2014; Stevens et al. 2016; Henriques et al. 2020; Stevens et al. 2024). SAMs are simpler in design and hence computationally inexpensive compared to full hydrodynamical simulations, making them ideal for simulating large volumes of the universe (Cowley et al. 2018; Lu et al. 2025) and exploring different physical models (Mutch et al. 2016; Yung et al. 2019a; Hutter et al. 2021; Cueto et al. 2024).

In numerical hydrodynamic simulations, baryonic matter is modelled as a fluid. The equations of gravity, hydrodynamics, thermodynamics, and optionally magnetism and radiative transfer, are solved for individual particles or cells. Subgrid models are used to model physical processes that occur on scales smaller than can be resolved, for example the formation and feedback processes of stars and black holes. The higher spatial resolution of hydrodynamical simulations allows for more realistic representations of environmental processes, morphology, and galaxy kinematics than SAMs (Mitchell et al. 2018; Pandya et al. 2020; Ayromlou et al. 2021). A consequence of this is increased computational expense, which leads to a strong trade-off between simulation resolution and volume.

Many comparison studies involving SAMs can be found in the literature, some solely focused on SAMs (De Lucia et al. 2010; Lu et al. 2014; Saghiiha et al. 2017) and others including hydrodynamical

simulations as a contrast, often with a view to understanding how the modelling in SAMs can be improved (Hirschmann et al. 2012; Monaco et al. 2014; Guo et al. 2016; Cui et al. 2018; Mitchell et al. 2018; Pandya et al. 2020; Ayromlou et al. 2021; Hadzhiyska et al. 2021; Yates et al. 2021b; Gabrielpillai et al. 2022; Lagos et al. 2025). To our knowledge, there has not been a comparison of different SAMs focused on the Epoch of Reionisation ( $z > 5$ ), though predictions by individual SAMs have certainly been made in this redshift regime (Yung et al. 2019a,b, 2020, 2021, 2022, 2024a; Lu et al. 2025; Vani et al. 2025; Somerville et al. 2025). Most models, be they hydrodynamical or semi-analytic, are calibrated on low-redshift ( $z < 3$ ) datasets. Going forward, it is likely that observational constraints from *JWST* will play a part in informing the development of galaxy formation models, either as a direct constraint in the calibration process, or as a consideration when looking to improve the physics in these models. Thus, the more we can understand how and why our models differ at high redshift, the better.

In this paper, we use the re-simulation strategy of the First Light And Reionisation Epoch Simulations (FLARES, Lovell et al. 2021; Vijayan et al. 2021) to perform a high-redshift ( $5 \leq z \leq 12$ ) comparison of the EAGLE hydrodynamics model (Crain et al. 2015; Schaye et al. 2015) and four SAMs – GALFORM (Baugh et al. 2019), L-GALAXIES (Yates et al. 2024), the Santa Cruz SAM (SC-SAM, Yung et al. 2024a) and SHARK (Lagos et al. 2024). The FLARES zoom simulations are specifically designed for studying galaxy formation and evolution at high-redshift. The fiducial FLARES suite, which features in previous FLARES publications, adopts the EAGLE model. The SAMs are run on merger trees extracted from a DMO simulation suite that uses the same zoom regions as the fiducial suite. These zoom regions are selected with a preference for highly overdense environments, so as to improve the statistics of massive galaxies. To obtain a globally representative sample, a weighting scheme is used to combine galaxy populations from the different regions. SAMs are not typically run on zoom simulations – as mentioned earlier, they do not require much computational resource, and can thus very feasibly be run on large DMO simulations. The efficiency gained by taking the zoom simulation approach is more meaningful when simulating with hydrodynamics. However, running the SAMs on the DMO suite allows us to compare the SAMs with the fiducial FLARES suite using the same region selection and volume, and ensures that the effective volume sampled is large enough for a robust comparison at high-redshift.

The structure of the paper is as follows: in Section 2, we introduce the models used in this analysis and provide an overview of how relevant physical processes are implemented in each model. In Section 3, we introduce the fiducial FLARES suite and the DMO simulation suite on which the SAMs are run. We also detail our procedure for running the SAMs. Section 4 contains our analysis of general galaxy properties predicted by the models, and in Section 5 we focus on the properties of passive galaxies, before concluding in Section 6.

## 2 MODEL DESCRIPTIONS

The models that feature in our analysis are EAGLE, GALFORM, L-GALAXIES, SC-SAM and SHARK. In this section, we specify their version, summarise how relevant physical processes are modelled, and list the observables used in their calibration.

### 2.1 EAGLE

The EAGLE hydrodynamics model is detailed in Crain et al. (2015) and Schaye et al. (2015). We use the AGNt9 model, which leads to

less frequent, more energetic AGN feedback events than the fiducial model. This model better reproduces the observed properties of hot gas in groups and clusters, while maintaining similar mass functions to the fiducial EAGLE model (Barnes et al. 2017b). This is particularly important for the overdense environments sampled in FLARES.

Radiative cooling and photoheating are modelled element-by-element using rates tabulated by Wiersma et al. (2009a). Star formation is modelled stochastically, with a dependence on pressure rather than density, following Schaye & Dalla Vecchia (2008). Since gas is not divided into atomic and molecular phases, a metallicity-dependent density threshold (Schaye 2004) is defined, above which star formation can occur. The stellar mass lost due to stellar winds and supernovae is distributed to neighbouring gas particles, with the exact amount depending on particle separation (Wiersma et al. 2009b). Stellar feedback is modelled as a stochastic injection of thermal energy into neighbouring gas particles when a stellar particle reaches an age of 30 Myr. Affected gas particles all experience a temperature increase of  $10^{7.5}$  K. Higher densities and lower metallicities lead to more energy being injected into the ISM per supernova event.

If a Friends-Of-Friends (FOF, Davis et al. 1985) halo does not already contain a black hole, it is seeded with one when it reaches a mass of  $M_{\text{FOF}} = 10^{10} h^{-1} M_{\odot}$ . The rate at which a black hole accretes mass is taken as the minimum of the Eddington accretion rate and the Bondi-Hoyle accretion rate (Bondi & Hoyle 1944) times an efficiency factor, whichever of the two is lower (see §4.6.2 of Schaye et al. (2015) for more detail). At each time step, the amount of energy stored in a ‘reservoir’ for AGN feedback is proportional to the black hole accretion rate. Only when the reservoir contains sufficient energy can feedback occur, similarly to stellar feedback, via the stochastic injection of thermal energy into neighbouring gas particles. The resulting temperature increase of each gas particle is  $\Delta T = 10^9$  K for the AGNdt9 model.

The model is calibrated at  $z = 0$ , with stellar feedback and black hole accretion tuned using the stellar mass function (SMF) and galaxy disk sizes, and AGN feedback tuned using the stellar-to-black hole mass relation (Crain et al. 2015).

## 2.2 GALFORM

We run the same version of GALFORM (Cole et al. 2000) used in Cowley et al. (2018); Baugh et al. (2019); Lu et al. (2025). The model is similar to that described in Lacey et al. (2016), with just an updated merger prescription and parameters tuned to the P-MILLENNIUM simulation (Baugh et al. 2019).

The cooling time is a characteristic timescale over which circumgalactic hot gas radiates away its thermal energy. It is calculated as in White & Frenk (1991), using the cooling function of Sutherland & Dopita (1993), but with a different halo gas density profile. The radius at which gas cools onto a galaxy (also known as the cooling radius) is the smaller of two quantities: 1) the radius at which the cooling time is equal to the time since the halo formation event (taken to occur every time a halo doubles in mass), and 2) the radius at which the time taken for a particle to fall to the halo centre under the effects of gravity (also known as free-fall time) is equal to the time since the halo formation event.

Star formation is modelled differently in the disk and spheroid. In the disk, cold gas is partitioned into atomic and molecular phases using the formulation by Blitz & Rosolowsky (2006), which depends on the midplane hydrostatic pressure of the disk, obtained using an approximation by Elmegreen (1993) (see Lagos et al. 2011 for more detail). In the spheroid, all gas is assumed to be in the molecular phase. Episodes of star formation in the spheroid, also known as

starbursts, are triggered by mergers and disk instabilities. The star formation rates (SFRs) in both the disk and spheroid are proportional to their respective molecular gas masses, by different tunable factors. Different stellar initial mass functions (IMFs) are assumed as well. In the disk, stars form with a Kennicutt (1983) IMF, such that the fraction of stellar mass instantaneously returned to the cold gas as a result of dying stars is  $R = 0.44$ . In the spheroid, a single power law IMF is used with its slope as a tunable parameter, leading to a top-heavy IMF with a slope of  $x = 1$  (c.f. Salpeter (1955)  $x = 1.35$ ) and an instantaneous stellar mass return fraction of  $R = 0.54$ . Stellar feedback ejects cold gas into an ejecta reservoir at a rate dependent on circular velocity.

A SMBH starts out with negligible mass and experiences its first significant growth during a galaxy’s first merger-triggered starburst (Malbon et al. 2007). When starbursts occur, a fraction of the cold gas in the spheroid is accreted by the SMBH. This ‘starburst mode’ accretion is the dominant channel for SMBH growth. A separate channel, known as ‘radio mode’ accretion (Bower et al. 2006; Croton et al. 2006), contributes little to the mass of a SMBH, but is associated with strong AGN feedback in the form of relativistic jets. Radio mode accretion occurs if: 1) hot gas cools slowly enough to be in quasi-hydrostatic equilibrium (determined by the ratio of the cooling time and free-fall time), and 2) the SMBH is sufficiently large, such that the power required to balance the radiative cooling luminosity of the hot gas can be produced at accretion rates much lower than the Eddington luminosity (assuming relativistic jets are only produced by low accretion rates). The power of these AGN jets is adjusted to balance the radiative cooling luminosity exactly.

When a galaxy becomes a satellite, it undergoes instantaneous ram pressure stripping – all hot gas associated with its halo is transferred to the halo of the new central. As such, satellites are unable to accrete cold gas. Subhalo positions are used to track satellite galaxies until the subhalos have been stripped of enough mass that they are no longer resolved ( $< 20$  particles). At this point, the galaxy becomes an orphan, and its merger timescale is calculated analytically, accounting for the effects of dynamical friction and tidal disruption using the prescription developed by Simha & Cole (2017).

GALFORM is calibrated using forward-modelled observables. Stellar SEDs are obtained using the Maraston (2005) stellar population synthesis (SPS) library, and dust is modelled self-consistently as molecular clouds embedded in a diffuse dust component, in a similar manner to the GRASIL spectrophotometric model (Silva et al. 1998; Lacey et al. 2016).

In the calibration process, primary constraints take priority over secondary constraints. On the list of primary constraints are the present-day optical and near-IR luminosity functions, present-day HI mass function, present-day morphological fractions, present-day black hole-bulge mass relation, near-IR luminosity functions from  $z = 0 - 3$ , sub-millimetre galaxy counts, far-IR galaxy counts, and far-UV luminosity functions of Lyman-break galaxies at  $z = 3$  and  $z = 6$ . Secondary constraints consist of the Tully-Fisher relation at  $z = 0$ , early- and late-type galaxy sizes at  $z = 0$ , and early-type galaxy stellar metallicities at  $z = 0$  (Lacey et al. 2016).

## 2.3 L-GALAXIES

We use the publicly available<sup>1</sup> Yates et al. (2024) version of L-GALAXIES, which builds on the Yates et al. (2021a) version by

<sup>1</sup> [https://github.com/LGalaxiesPublicRelease/LGalaxies2020\\_PublicRepository/tree/Yates2023](https://github.com/LGalaxiesPublicRelease/LGalaxies2020_PublicRepository/tree/Yates2023)

implementing binary stellar evolution and a detailed dust model. [Yates et al. \(2021a\)](#) is a version of L-GALAXIES 2020 ([Henriques et al. 2020](#)) with a modified stellar feedback scheme that increases the fraction of metals directly ejected into the circumgalactic medium (CGM), as opposed to mixing with the ISM. This leads to an improved agreement with low-redshift observations of mass-metallicity relations and radial metallicity profiles for both stars and gas, while retaining previous agreement with other key properties.

The cooling time is calculated following [White & Frenk \(1991\)](#), using the cooling function of [Sutherland & Dopita \(1993\)](#). The cooling radius is given by the radius at which the cooling time is equal to the halo dynamical time. Two accretion modes are defined – hot (cold) mode accretion occurs when the cooling radius is smaller (larger) than the halo radius, which is defined as  $R_{200c}$ .

L-GALAXIES 2020 (and its offshoots) adopts a spatially-resolved treatment for gas and stellar disks, using layers of concentric rings ([Fu et al. 2013](#)). In each ring, cold gas is divided into atomic and molecular phases using a fitting formula by [McKee & Krumholz \(2010\)](#), based on work by [Krumholz et al. \(2009\)](#), who model the fraction of molecular hydrogen as a function of metallicity and the local surface density of cold gas. The star formation surface density is then proportional to the surface density of molecular hydrogen. Mergers can lead to starbursts, with the stellar mass formed in each ring dependent on the baryonic mass ratio of the merging galaxies and the cold gas mass in the ring ([Somerville et al. 2001](#)). Stellar feedback, dependent on the maximum circular velocity, can reheat cold gas into the hot halo, and also eject hot gas into the ejecta reservoir, if there is energy left over from heating the cold gas. The release of energy and metals by stellar populations is tracked separately for each ring, assuming a [Chabrier \(2003\)](#) IMF.

SMBHs are seeded with negligible mass. SMBH growth in L-GALAXIES occurs primarily through ‘starburst mode’ accretion, triggered by galaxy mergers, when cold gas is driven towards the central region of the new system. SMBHs also grow via inflows of gas from the hot halo in ‘radio mode’ accretion. The radio mode accretion rate is proportional to the hot halo mass and SMBH mass by a tunable factor. This is almost identical to the model presented in [Croton et al. \(2006\)](#), but with no dependence on  $H(z)$ , leading to enhanced accretion at low redshift. Radio mode feedback is the only mode of AGN feedback in L-GALAXIES, and is modelled by using a fraction  $\epsilon_{\text{heat}} = 0.1$  of the energy obtained from radio mode accretion to suppress the cooling of hot gas. One could consider that other forms of AGN feedback may be accounted for in the modelling of stellar feedback (this same perspective could be applied to the highly similar modelling of AGN feedback in GALFORM as well).

Subhalo positions are used to track satellite galaxies until the subhalos become sub-resolution ( $< 20$  particles). Satellites are only subject to tidal and ram pressure stripping if situated within the virial radius of their host halo. Tidal forces are modelled by the removal of hot gas beyond a minimum radius in proportion to the amount of dark matter being lost from the subhalo. Satellites situated within larger parent halos with masses greater than  $\sim 10^{14} M_{\odot}$  are additionally affected by ram pressure stripping (note, though, that halos do not reach this size at the redshifts probed in this paper). Hot gas removed from a satellite via the aforementioned mechanisms is transferred to the hot gas halo of the central galaxy, and any hot gas that remains is allowed to cool onto the satellite. By construction, orphan galaxies do not have any associated dark matter or hot gas. Their merger timescale is calculated following [Binney & Tremaine \(1987\)](#), but they may be tidally disrupted beforehand if their baryonic density is less than the dark matter density of the host halo.

L-GALAXIES 2020 is calibrated using observations of the stellar

mass function at  $z = 0$  and  $z = 2$ , passive fractions at  $z = 0$  and  $z = 2$ , and the HI mass function at  $z = 0$ . [Yates et al. \(2021a\)](#) find that differences in the general galaxy properties between their new model and L-GALAXIES 2020 are small at  $z < 2$ . Thus, the [Yates et al. \(2021a\)](#) and [Yates et al. \(2024\)](#) models are not recalibrated – they use the same default parameter values as L-GALAXIES 2020.

## 2.4 Santa Cruz SAM

We use the same version of SC-SAM as in [Yung et al. \(2024a\)](#). Details of the model can be found in [Somerville et al. \(2008, 2015\)](#); [Yung et al. \(2024a\)](#).

As in GALFORM and L-GALAXIES, the cooling time is calculated using the formula by [White & Frenk \(1991\)](#) and the temperature- and metallicity-dependent cooling function of [Sutherland & Dopita \(1993\)](#). Similarly to L-GALAXIES, the cooling radius is defined as the radius within which the cooling time is equal to the halo dynamical time. When the cooling radius is less (greater) than the virial radius of the halo, gas accretion occurs in hot (cold) mode.

Cold gas is partitioned into atomic, molecular and ionised components, using fitting formulae based on the results of simulations by [Gnedin & Kravtsov \(2011\)](#), which depend on gas phase metallicity, gas phase surface density and UV-background. Star formation efficiency is assumed to increase with molecular hydrogen surface density, using a double power law motivated by observations (for details, see [Somerville et al. 2015](#)). Galaxy mergers lead to episodes of star formation known as starbursts, which have a star formation efficiency and timescale determined by the mass ratio and gas fraction of the merging galaxies, based on predictions from hydrodynamic simulations by [Robertson et al. \(2006\)](#) and [Hopkins et al. \(2009\)](#) ([Somerville et al. 2008](#)). A universal [Chabrier \(2003\)](#) IMF is assumed, with a recycled fraction of  $R = 0.43$ . The outflow rate of cold gas due to supernova feedback is assumed to depend on the circular velocity of the galaxy. Some of the ejected gas is transferred to the hot halo, and the remainder is deposited in the ejecta reservoir.

In SC-SAM, host halos are seeded with a black hole of mass  $M_{\text{BH}} = 10^4 M_{\odot}$ . The treatment of black hole growth resulting from galaxy mergers is informed by the results of hydrodynamic simulations of binary mergers of idealized galaxies. Just after a merger, the SMBH mass of a galaxy is equal to the summed SMBH masses of its progenitors. The SMBH then grows at the Eddington rate until reaching a critical mass, at which point it produces feedback in the form of a pressure-driven outflow – we will call this ‘wind mode’ feedback. A radiatively-efficient ‘blow-out’ phase occurs, where the SMBH accretion rate declines as a power law, following light curves from simulations by [Hopkins et al. \(2006\)](#). Disk instabilities are another channel for rapid SMBH growth. In such cases, a fraction  $f_{\text{BH,disk}} = 0.001$  of the disk mass is allowed to be accreted onto the black hole, over a timescale guided by the light curves of [Hopkins et al. \(2006\)](#). When a halo is cooling in hot mode, radio mode accretion occurs via a cooling flow from the hot halo, assuming Bondi-Hoyle accretion (the exact strength of which is tuned by a free parameter) and the isothermal cooling flow model of [Nulsen & Fabian \(2000\)](#). The associated radio mode feedback is modelled by using a fraction of the energy gained through radio mode accretion to offset cooling from the hot halo to the ISM.

Satellites are modelled analytically rather than relying on dark matter substructure, i.e. all satellites are treated as orphans. Like GALFORM, satellite galaxies do not accrete new cold gas. The merger timescale of a satellite is calculated using an updated version of the Chandrasekhar formula for dynamical friction that considers the energy and angular momentum of the satellite’s orbit, as well as tidal

stripping effects on subhalos (Boylan-Kolchin et al. 2008; Somerville et al. 2008). Satellites lose between 30 – 40% of their mass every orbital period, and are considered to be tidally disrupted if their mass is less than that contained within the Navarro et al. (1996) scale radius at the time of infall. The cold gas in tidally-disrupted satellites is transferred to the hot gas reservoir of the central galaxy.

The model parameters used here are those obtained in the study by Gabrielpillai et al. (2022), with the following  $z = 0$  quantities used as constraints: the stellar mass function, stellar-to-halo mass relation, stellar mass-metallicity relation, cold gas fraction-to-stellar mass relation for disk galaxies, and black hole mass-bulge relation.

## 2.5 SHARK

We use the publicly available<sup>2</sup> SHARK 2.0, which is an updated version of the original SHARK 2.0 model described in Lagos et al. (2024). The full list of changes can be found in Oxland et al. (2025; submitted). We include a description of the updates, where relevant.

The cooling time is computed as in White & Frenk (1991), using tabulated cooling functions obtained with CLOUDY (Ferland et al. 1998). Cooling is modelled using the Croton et al. (2006) model, with the same definitions of accretion modes as L-GALAXIES and SC-SAM – hot (cold) accretion takes place when the cooling radius is smaller (greater) than the virial radius of the halo.

Star formation in the disk is calculated similarly to GALFORM, using the Blitz & Rosolowsky (2006) model to calculate the ratio of molecular to atomic hydrogen, and with the hydrostatic mid-plane pressure calculated following Elmegreen (1993). The SFR surface density is proportional to the molecular hydrogen surface density. Star formation in the spheroid is modelled as starbursts, triggered by galaxy mergers or disk instabilities. The same gas partitioning recipe is used in the disk and spheroid. However, the star formation efficiency in the spheroid is boosted by a multiplicative factor, tuned to observations. A Chabrier (2003) IMF is used throughout, with a recycled fraction of  $R = 0.46$ . Stellar feedback causes gas to be expelled from a galaxy, some of which is also expelled from the halo. Feedback is modelled following the implementation of Lagos et al. (2013), whereby the rate at which gas is expelled from a galaxy is proportional to circular velocity. Unlike in Lagos et al. (2024), stellar feedback is dependent on the age of the universe rather than  $(1+z)$  (see Equation 29 in Lagos et al. (2018)). This change was made to improve supernova feedback at high redshifts.

SMBHs are seeded with a mass of  $M_{\text{BH}} = 10^4 h^{-1} M_{\odot}$  in halos with a minimum mass of  $M_{\text{halo}} > 10^{10} h^{-1} M_{\odot}$ . The accretion rate of a SMBH when its host galaxy is undergoing hot mode accretion is computed following Croton et al. (2016), assuming a Bondi-Hoyle-like accretion mode that can be tuned by a free parameter. Black holes also grow when starbursts occur, according to the prescription by Kauffmann & Haehnelt (2000), with the accreted mass proportional to that of the cold gas reservoir. A normalised accretion rate is obtained by dividing the total accretion rate by the Eddington accretion rate. This is used to differentiate between accretion regimes, in order of decreasing normalised accretion rate: Super-Eddington (SE) accretion; a thin disk (TD) regime (Shakura & Sunyaev 1973); a high accretion rate advection-dominated accretion flow (ADAF) regime, in which electrons are predominantly heated by viscous heating; a low accretion rate ADAF regime, in which electrons are predominantly heated by ion-heating. AGN bolometric luminosities are calculated

following Griffin et al. (2019) and Griffin et al. (2020), with the calculation depending on which of four accretion regimes the black hole is in. AGN feedback is modelled in two modes, known as ‘jet mode’ and ‘wind mode’. Unlike in other SAMs, these modes are not directly related to the gas accretion mode. Jet mode feedback occurs when a hot gas halo has formed, according to conditions defined in Correa et al. (2018). The jet power is calculated following Meier (2002), who differentiates between AGN in an ADAF-dominated regime and AGN with higher accretion rates, using the aforementioned classification. The total accretion rate of the SMBH is used to compute the jet power, and a fraction of the jet power is used to counteract the cooling of hot gas. Wind mode feedback is triggered when the bolometric luminosity of the AGN is above a critical value such that radiation pressure is able to deposit momentum onto dust grains, driving galactic winds.

Satellites in SHARK are tracked using the information of their subhalo. Stars and cold gas in satellites are tidally stripped following a formula presented in Errani et al. (2015) that depends on the ratio between the subhalo mass at present and its value at infall. Ram pressure stripping is modelled following the results of hydrodynamical simulations (Font et al. 2008; McCarthy et al. 2008), and affects both the hot and cold gas components in satellites, with different stripping radii assumed for each component. Satellite galaxies are still able to accrete cold gas from their hot halo. If the satellite contains an AGN in jet mode, any AGN feedback power leftover from counteracting the cooling of hot gas is used to heat the hot gas atmosphere associated with the central galaxy. When the satellite becomes an orphan, its cold gas component is subject to ram pressure stripping as per usual, while all of its hot gas is immediately moved to the hot gas reservoir of the central galaxy. The merger timescale of the orphan is obtained using a formula by Poulton et al. (2021), which compared to other models has a reduced dependence on the subhalo-to-host halo mass ratio and differentiates between galaxies within and beyond the virial radius of the host halo. Note that since the initial release of SHARK 2.0 in Lagos et al. (2024), a new parameter (`alpha_cold`) has been introduced to control the stripping of cold gas. Additionally, parameters controlling the stripping of hot gas have been updated so that stripping occurs more gradually.

An additional update to this version of SHARK is the inclusion of fixes at the SAM level to deal with numerical artefacts in merger tree data (Chandro-Gómez et al. 2025).

The version of SHARK we use is calibrated manually and fine-tuned using an automated parameter search, via the `optim` Particle Swarm Optimisation (PSO) package in SHARK, with the stellar mass functions at  $z = 0, 1, 2, 4$  and the HI mass function at  $z = 0$  used as direct constraints.

## 3 METHODS

In this section, we introduce the simulation suites that feature in our analysis and detail our procedure for running the SAMs.

### 3.1 First Light And Reionisation Epoch Simulations

We distinguish between the FLARES simulation suite run with the EAGLE hydrodynamics model and the FLARES simulation suite run with dark matter only by labelling the former as the fiducial suite and the latter as the DMO suite. Note that all mentions of the EAGLE model in this paper reference results from the fiducial FLARES suite, rather than the flagship EAGLE simulations. However, to facilitate

<sup>2</sup> <https://github.com/ICRAR/shark>

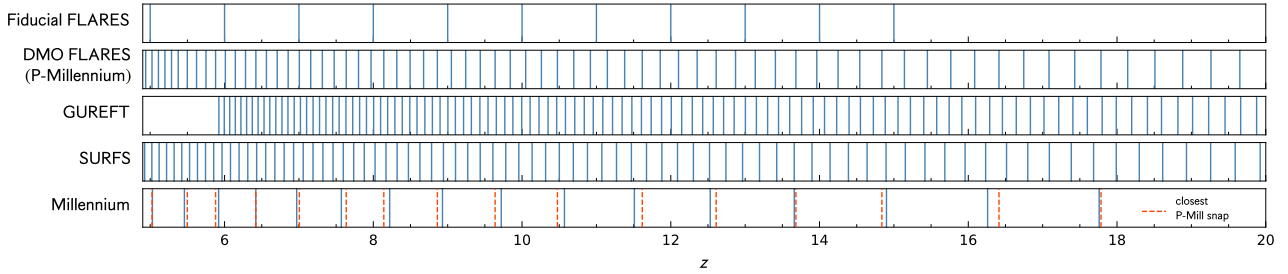


**Figure 1.** Snapshot cadence used in various simulations, from top to bottom: the fiducial FLARES suite, the FLARES DMO suite (resimulated from the parent simulation with the same cadence as the P-MILLENNIUM simulation (Baugh et al. 2019)), the GUREFT simulation suite (Yung et al. 2024b), the SURFS simulation suite (Elahi et al. 2018), and the MILLENNIUM-I and II simulations (Springel et al. 2005; Boylan-Kolchin et al. 2009). The dashed red lines in the bottom-most row represent the snapshots used when running L-GALAXIES on the FLARES DMO suite – these are subsampled from the SAM DMO snapshot cadence (same as P-MILLENNIUM).

comparison between the different models in this paper, we will refer to galaxies in the fiducial FLARES suite as EAGLE galaxies.

The fiducial FLARES suite is introduced in Lovell et al. (2021) and Vijayan et al. (2021). The suite comprises 40 spherical zoom-in simulations, each of radius  $14 h^{-1}\text{Mpc}$  at  $z = 4.67$ . The zoom regions are selected from a large  $(3.2 \text{ cGpc})^3$  DMO parent simulation (Barnes et al. 2017a), allowing a wide range of overdensities to be sampled ( $\delta = -0.497 \rightarrow 0.970$ ). Highly overdense regions are preferentially selected in order to simulate a greater number of massive galaxies (Chiang et al. 2013; Lovell et al. 2018). The regions are selected at  $z = 4.67$ , when density perturbations are only mildly non-linear. This helps to ensure that the rank ordering of overdensities is still preserved at high-redshift, ensuring the weighting scheme remains robust. The hydrodynamics model used is the AGNdT9 variant of the EAGLE subgrid model (Crain et al. 2015; Schaye et al. 2015), as mentioned in §2.1. The fiducial FLARES suite has the same resolution as the flagship EAGLE run, with a dark matter particle mass  $M_{\text{DM}} = 9.7 \times 10^6 M_{\odot}$ , an initial gas particle mass  $M_{\text{gas}} = 1.8 \times 10^6 M_{\odot}$  and a softening length of 2.66 kpc. Outputs are stored at integer redshift, from  $z = 15 \rightarrow 5$ .

The SAM DMO suite used in this study is a resimulation of the same 40 zoom regions, as in the fiducial FLARES suite, using a dark matter particle mass of  $M_{\text{DM}} = 8.36 \times 10^7 M_{\odot}$  and a softening length of 4.32 kpc. This particle mass was chosen as a resolution at which the four SAMs in this study are sufficiently converged. More information on the convergence tests is provided in §3.2.2 and §B. Outputs are stored at the same redshifts as in the P-MILLENNIUM simulation (Baugh et al. 2019). This output frequency, much higher than the fiducial FLARES suite, is necessary to accurately capture the halo merger histories required for SAMs. The first two rows of Figure 1 show the output snapshots of the fiducial and DMO suites. More discussion on the choice of snapshot cadence can be found in §3.2.3.

As our region selection contains many more highly overdense regions than one would find in a periodic box of the same simulated volume, the zoom regions on their own do not provide a statistical representation of galaxies in the universe. To study the global population of galaxies, we combine the statistics of individual regions using a weighting scheme that reduces the contribution from galaxies in rarer regions (i.e. highly overdense and underdense ones). Since the same region selection is used in the fiducial and DMO suites, the same weightings apply. All composite distribution functions and scaling relations shown in this paper are obtained using this weighting scheme. More detail on how the weights are obtained can be found in Lovell et al. (2021).

The fiducial and DMO suites assume a Planck Collaboration et al. (2014) cosmology, with  $\Omega_{\Lambda} = 0.693$ ,  $\Omega_m = 0.307$ ,  $h = 0.6777$ .

### 3.2 Running the SAMs

We note that the SAMs are not recalibrated for this analysis, and that the predictions of a SAM can be sensitive to several factors: cosmology, the resolution of the DMO simulation from which merger histories are obtained, the halo-finding and merger tree codes used, and the time resolution of the merger histories. Here, we detail our methodology, and explain where relevant how we have checked for convergence.

#### 3.2.1 Halo-finding and merger tree codes

GALFORM and SHARK are run on the same set of merger trees, obtained using the SUBFIND (Springel et al. 2001) halo-finder, D-TREES (Jiang et al. 2014) merger tree builder and DHALO (Jiang et al. 2014) post-processing tool. L-GALAXIES is run on merger trees obtained using the SUBFIND and LHALOTREE (Springel et al. 2005) algorithms present in the GADGET-4 (Springel et al. 2021) code. SC-SAM is run on merger trees obtained using the ROCKSTAR (Behroozi et al. 2013a) and CONSISTENT TREES (Behroozi et al. 2013b) algorithms.

Using the same pipeline for each SAM would lead to a cleaner comparison of the modelling. However, the performance of each SAM likely depends, to varying extent, on the algorithms used. Gabrielpilai et al. (2022) mention that SC-SAM performs less well on SUBLINK (Rodríguez-Gomez et al. 2015) merger trees, due to differences in the number of identified mergers. Lee et al. (2014) find that using different tree codes, D-TREES and CONSISTENT TREES included, can lead to notable differences in the mean star formation histories (SFHs), satellite numbers and galaxy merger rates predicted by a SAM. On the other hand, Gómez et al. (2022) show that predictions by GALFORM are robust to the use of different algorithms, for the same underlying DMO simulation. Chandro-Gómez et al. (2025) find that SAMs relying on subhalo properties, such as previous versions<sup>3</sup> of SHARK, are susceptible to numerical issues in merger tree data. In contrast, halo-based SAMs, such as GALFORM, are less affected.

Since the focus of this paper is on the physical predictions of different SAMs at high-redshift, rather than the details of their modelling,

<sup>3</sup> The updated version of SHARK includes fixes at the SAM level to reduce numerical artefacts in merger tree data.

SAM	Version	DMO	$M_{\text{DM}} (M_{\odot})$	Volume ( $\text{cMpc}^3$ )	$\sigma_8$	$h$	$\Omega_m$
(All)	(See below)	FLARES DMO	$8.36 \times 10^7$	$40 \times 33.3^3$	0.829	0.678	0.307
GALFORM	Baugh et al. (2019)	P-Millennium	$1.56 \times 10^8$	$800^3$	0.829	0.678	0.307
L-Galaxies	Yates et al. (2024)	Millennium I	$1.43 \times 10^9$	$714^3$	0.829	0.673	0.315
		Millennium II	$1.14 \times 10^7$	$143^3$			
SC-SAM	Yung et al. (2024a)	GUREFT-05	$1.5 \times 10^4$	$7.4^3$	0.823	0.678	0.308
		GUREFT-15	$4.0 \times 10^5$	$22.1^3$			
		GUREFT-35	$5.0 \times 10^6$	$53.6^3$			
		GUREFT-90	$8.5 \times 10^7$	$132^3$			
SHARK	Lagos et al. (2024)	SURFS	$3.27 \times 10^8$	$311^3$	0.815	0.675	0.312

**Table 1.** Columns contain, from left to right: (1) the name of the SAM, (2) the publication associated with the model of the SAM, (3) the name of the DMO simulation on which the SAM was run in the publication stated in (2), (4) the particle mass in the DMO simulation, (5) the volume of the DMO simulation, (6) the amplitude of the linear power spectrum on scales of  $8 h^{-1} \text{Mpc}$ , (7) the reduced Hubble parameter, (8) the present-day energy density of matter in units of the critical density. The 40 regions in the FLARES DMO suite are spherical, but their individual volume is expressed as a cubed length to facilitate comparison with the other simulations.

we endeavour to run halo-finding and tree-building algorithms that have been used to run the SAMs in prior studies. In the case of GALFORM, L-GALAXIES and SC-SAM, we use the same codes employed in their calibration runs (Baugh et al. (2019), Henriques et al. (2020) and Gabrielpillai et al. (2022), respectively). SHARK is an exception, as we use SUBFIND+D-TREES+DHALO in this analysis, as was done in D’Silva et al. (2025) and Lagos et al. (2025). This is different from the HBT-HERONS+DHALO pipeline employed in calibrating the SHARK model (Oxland et al., submitted).

### 3.2.2 Particle resolution

The fourth column in Table 1 shows the particle mass of the DMO simulation(s) on which the calibrated model of each SAM is run. Both L-GALAXIES and SC-SAM are calibrated to work at more than one resolution. We list these simulations to indicate the range of resolutions at which the models can be applied, guided by previous work. That said, it is not strictly true that the SAMs are fully converged for all properties in the stated resolution range. For example, gas-phase metallicities in L-GALAXIES are not fully converged between the MILLENNIUM-I and II resolutions (Yates et al. 2024).

We run detailed tests to determine the resolutions at which the SAMs are sufficiently converged, considering the galaxy properties studied in Section 4. A description of the test results can be found in Section B of the appendix. In short, to identify a common particle mass that works for the SAMs, we rerun the FLARES DMO suite at different resolutions, using a particle mass of  $1.15 \times 10^7$ ,  $8.36 \times 10^7$ ,  $1.58 \times 10^8$  and  $3.22 \times 10^8 M_{\odot}$  – these approximately correspond to the MILLENNIUM-II, GUREFT-90, P-MILLENNIUM and SURFS resolutions, and serve as benchmarks for L-GALAXIES, SC-SAM, GALFORM and SHARK respectively. We run all four SAMs at these resolutions and assess convergence at a given resolution by comparing the predictions of each SAM with those of its benchmark run. Where possible, we also compare with previously published results. We find that a particle mass of  $8.36 \times 10^7 M_{\odot}$ , similar to that of GUREFT-90, works well across all SAMs.

### 3.2.3 Snapshot cadence

GALFORM, SC-SAM and SHARK are run on merger trees constructed using the full set of snapshots stored from the FLARES DMO suite. As mentioned in §3.1, outputs of the DMO suite are saved at the same redshifts as in the P-MILLENNIUM simulation, ensuring a high

enough time resolution to resolve the merger histories of halos (Baugh et al. 2019). The GUREFT and SURFS simulations, used in the calibration runs of SC-SAM and SHARK respectively, have a similarly high time resolution (see second, third and fourth rows of Figure 1). L-GALAXIES is calibrated on the MILLENNIUM-I and II simulations, which have a coarser time resolution at high-redshift. To maintain consistency with previous works, we run L-GALAXIES on a sub-sample of the DMO outputs by constructing merger trees from snapshots closest in redshift to the output snapshots in the MILLENNIUM-I and II simulations (dashed red lines in Figure 1).

### 3.2.4 Cosmology

The SAMs are run assuming the same cosmology as FLARES (see §3.1). All SAMs adopt a similar  $\Lambda$ CDM Planck cosmology to the fiducial FLARES suite in their calibration runs (see last three columns of Table 1). Hence, issues of convergence arising from the use of different cosmologies are likely to be minimal.

## 3.3 Measuring galaxy properties

In the fiducial FLARES suite, a FOF algorithm (Davis et al. 1985) is used to group particles into halos. Substructure, which includes galaxies, is then identified using the SUBFIND (Springel et al. 2001) algorithm. Galaxy properties are computed using particles situated within a 30 pkpc (physical kpc) radius of the most bound particle in each substructure. The star formation rate (SFR) of a galaxy is averaged over the most recent 20 Myr. Throughout this work, we impose a stellar mass criteria of  $\log_{10}(M_{\star}/M_{\odot}) > 8$  on EAGLE galaxies, which roughly translates to the requirement that galaxies contain at least 50 star particles.

In the SAMs, galaxy properties are summed over spheroid and disk components (where split). The timescale over which the SFR is measured,  $t_{\text{SFR}}$ , differs across SAMs. For SC-SAM, we choose to use  $t_{\text{SFR}} = 20$  Myr. In L-GALAXIES, we calculate the SFR from the output SFHs, and obtain a timescale of  $t_{\text{SFR}} = 23.7, 24.1, 13.5, 16.4, 20.6, 25.1$  Myr at  $z = 5, 6, 7, 8, 9, 10.5$ , respectively. In GALFORM and SHARK, the SFR is averaged over the time between the current and previous snapshots, such that  $t_{\text{SFR}} = 24.6, 26.8, 21.4, 17.5, 15.6, 12.5$  Myr at  $z = 5, 6, 7, 8, 9, 10.5$ , respectively. SAMs can probe relatively lower baryon masses at fixed DM resolution – we include all galaxies in halos with at least 20 DM particles, which corresponds to halos with mass  $M_{\text{halo}} \geq 1.67 \times 10^9 M_{\odot}$ .

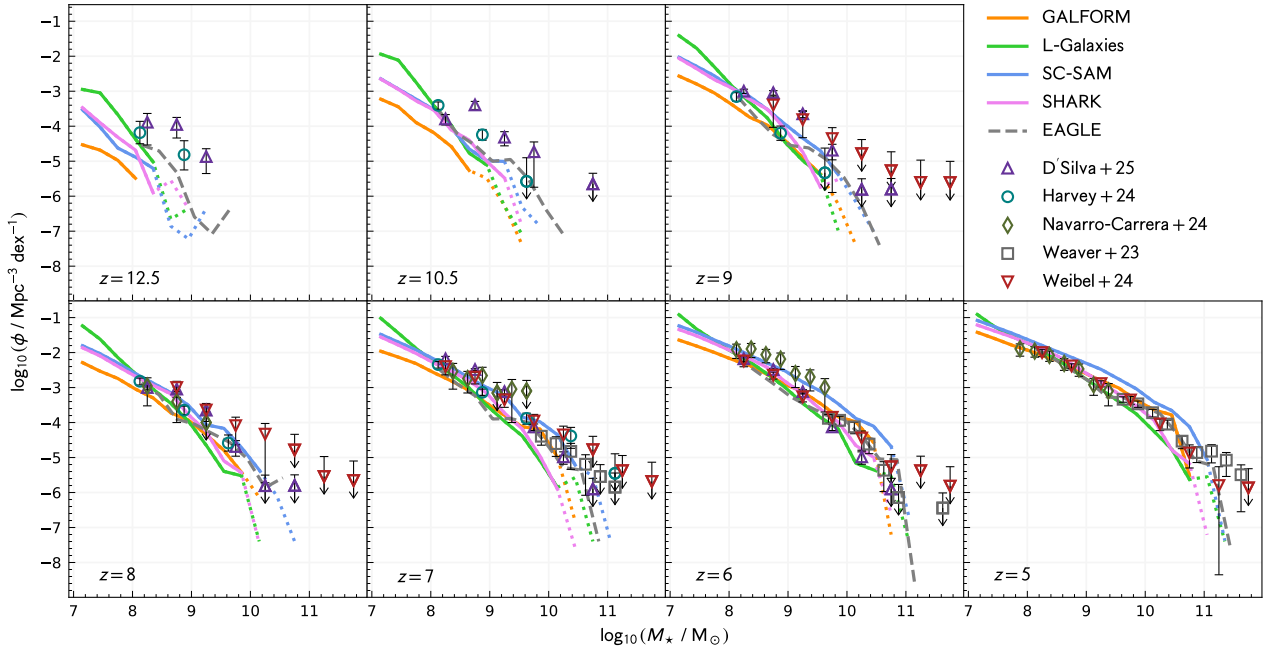


**Figure 2.** Stellar mass function predicted by the four SAMs (solid lines, or dotted to denote bins containing fewer than 10 galaxies) and EAGLE (dashed grey line). A stellar mass cut of  $M_{\star} > 10^8 M_{\odot}$  is applied to the EAGLE results. As the outputs of the fiducial FLARES suite are saved at integer redshift, the EAGLE predictions in the  $z = 10.5$  and  $z = 12.5$  panels are in fact at  $z = 10$  and  $z = 12$  respectively. Observations are plotted as symbols with error bars.

The halo masses shown in our analysis are defined differently in the models. GALFORM and SHARK use the DHALO (Jiang et al. 2014) definition of halo mass, SC-SAM use the Bryan & Norman (1998) definition based on virial mass, and both L-GALAXIES and the fiducial FLARES suite (i.e. EAGLE) use  $M_{200c}$ . We find that the HMFs obtained with the different halo definitions are very similar, and thus unlikely to affect the conclusions of our analysis.

## 4 PHYSICAL PROPERTIES

We now turn to the model predictions, focusing in this section on general trends in physical properties.

### 4.1 Stellar mass function

The redshift evolution of the stellar mass function (SMF) is shown in Figure 2, alongside recent measurements utilising *JWST* NIR-Cam data (Harvey et al. 2024; Navarro-Carrera et al. 2024; Weibel et al. 2024b; D'Silva et al. 2025) and the COSMOS2020 catalogue (Weaver et al. 2023).

Comparing the models, we find that L-GALAXIES has a relatively steep SMF, predicting a large number of low-mass galaxies ( $\log_{10}(M_{\star}/M_{\odot}) < 8$ ), especially at the highest redshifts, while also predicting fewer high-mass galaxies ( $\log_{10}(M_{\star}/M_{\odot}) > 10$ ). At  $z \leq 9$ , SC-SAM tends to have the highest SMF of the models, with GALFORM sitting  $\sim 0.3$  dex lower across the range of stellar masses probed. SHARK predicts numbers of high-mass galaxies in between that of GALFORM and L-GALAXIES, and has a similar slope to SC-SAM at lower stellar masses. As for the EAGLE SMF, it has a steep slope initially, resembling that of L-GALAXIES at  $\log_{10}(M_{\star}/M_{\odot}) < 9$ . As stellar mass increases, it follows the higher GALFORM SMF more closely.

All in all, the spread of predictions from the models is generally consistent with observational constraints. SC-SAM appears to slightly overestimate the SMF at  $z = 5$ . At first glance, L-GALAXIES tends to slightly under-predict the number of high-mass galaxies ( $\log_{10}(M_{\star}/M_{\odot}) > 10$ ) relative to the observations. However, we find that the discrepancy is no longer significant after adding a small margin of error to the stellar masses, to account for Eddington bias (see appendix). At the highest redshifts ( $z > 10$ ), measurements by Harvey et al. (2024) and D'Silva et al. (2025) suggest a higher SMF than predicted by most models, in particular GALFORM, which has the lowest SMF in this redshift regime.

We note that the assumptions made in converting between observed data and galaxy properties may strongly affect our conclusions. Although GALFORM predicts the fewest galaxies at  $z > 10$ , Lu et al. (2025) show that GALFORM is within the range of observations of the UVLF at  $z = 10$ . This may be due to a combination of the extremely top heavy IMF used by GALFORM for starbursts, as well as the forward-modelling choices made in Lu et al. (2025). It is also worth mentioning that observational constraints are less robust as redshift increases. Harvey et al. (2024) find that for their  $z \sim 10.5$  galaxy sample, stellar masses can increase by  $> 1$  dex when switching from their fiducial parametric SFH model to a non-parametric model. They also find that using the redshift-dependent, top heavy IMF by Steinhardt et al. (2023) reduces their estimated stellar masses at  $z > 8$  by 0.3 – 0.5 dex, with a greater reduction at higher redshift.

### 4.2 Stellar-to-halo mass relation

The first row of Figure 3 shows the stellar-to-halo mass relation (SHMR) of central galaxies, as a function of halo mass. We find little redshift evolution in the model predictions, except that they extend to higher halo masses as redshift decreases, as a result of hierarchical structure formation. L-GALAXIES tends to populate low-mass halos

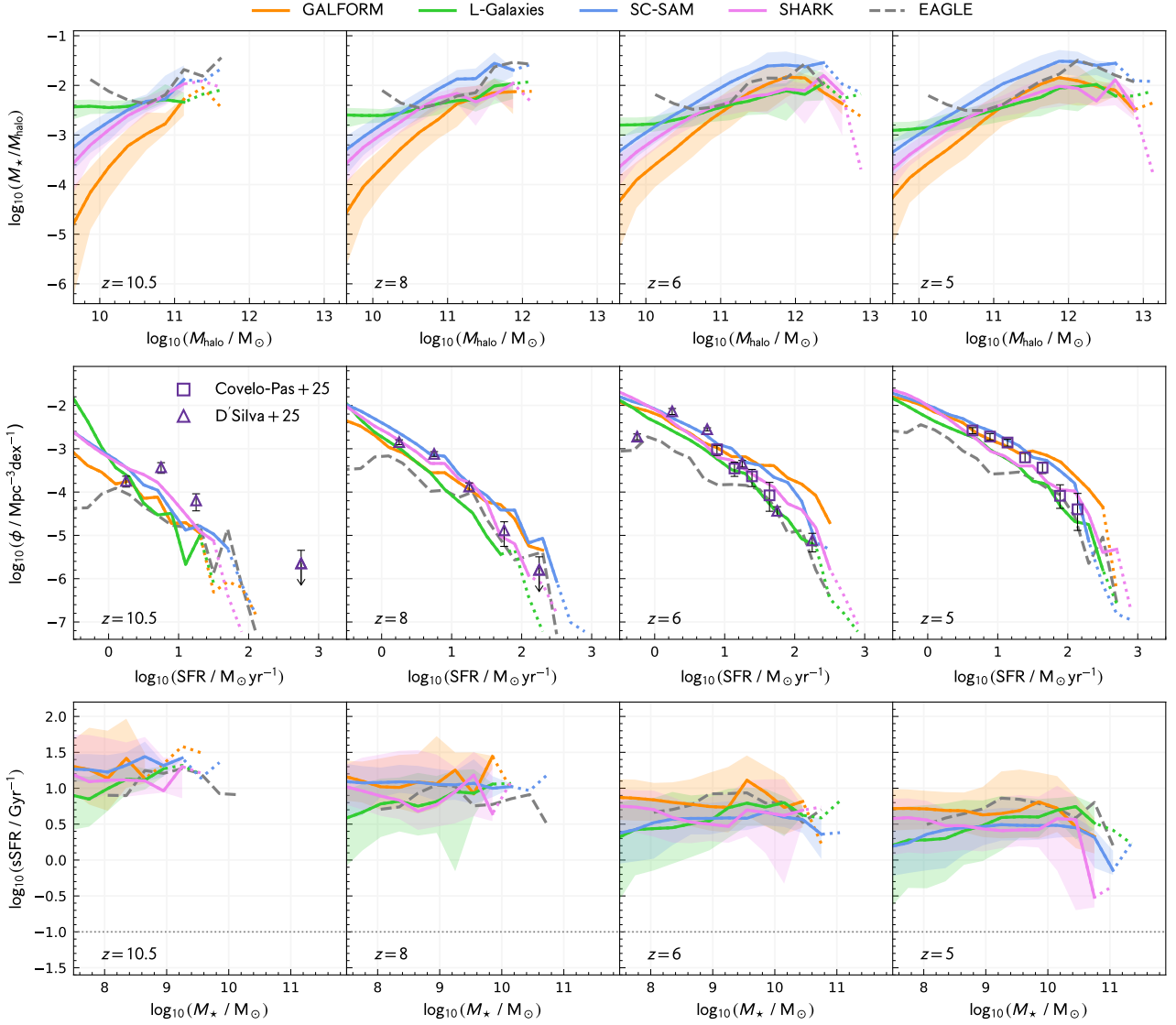


**Figure 3.** Each row shows a different quantity predicted by the four SAMs and EAGLE across a range of redshifts. From top to bottom: stellar-to-halo mass relation, SFR distribution function, star-forming main sequence. Note that a stellar mass cut of  $M_{\star} > 10^8 M_{\odot}$  is applied to the EAGLE results, and that the EAGLE predictions at  $z = 10.5$  are at  $z = 10$ , as outputs of the fiducial FLARES suite are saved at integer redshift. For the SAMs, dotted lines denote bins containing fewer than 10 galaxies. Shaded regions denote the  $1\sigma$  range of the SAMs. The dotted horizontal line in the final row marks the sSFR threshold below which galaxies are considered passive (relevant to §5).

( $\log_{10}(M_{\text{halo}}/M_{\odot}) < 10$ ) with the most massive galaxies. However, compared to other models, L-GALAXIES predicts a slower growth of stellar mass as halo mass increases. This explains the steep SMF that we saw previously. At  $\log_{10}(M_{\text{halo}}/M_{\odot}) > 10.5$ , it is generally SC-SAM that predicts the highest stellar masses for a given halo mass, likely due to the assumption of a steeper slope for the Kennicutt–Schmidt relation (Kennicutt 1989) above a critical gas mass density (Somerville et al. 2015; Yung et al. 2019b). GALFORM has the steepest SHMR, predicting the lowest stellar masses in the smallest halos, and catching up to the other models at  $\log_{10}(M_{\text{halo}}/M_{\odot}) = 11$ . At  $z \leq 8$ , the EAGLE SHMR tends to sit between the GALFORM and SC-SAM relations, with an initial gradient close to that of GALFORM, but eventually reaching slightly higher stellar masses as halo mass increases. Note that the increased stellar-to-halo mass ratio at low halo masses is due to the  $M_{\star} > 10^8 M_{\odot}$  cut applied to the EAGLE pre-

dictions. At the highest halo masses ( $\log_{10}(M_{\text{halo}}/M_{\odot}) > 11.5$ ), the stellar-to-halo mass ratios predicted by EAGLE, GALFORM, SC-SAM and SHARK increase more gradually. In GALFORM, there is a clear downturn in the relation, as AGN feedback starts to suppress the growth of massive galaxies. On the other hand in L-GALAXIES, stellar mass increases at high halo masses without turning over.

### 4.3 Star formation rates

The second row of Figure 3 shows the star formation rate function (SFRF) predicted by the models. At  $z \leq 8$ , the SFRFs are fairly similar at lower SFRs, differing by not more than  $\sim 0.5$  dex at  $\text{SFR} < 10 M_{\odot}\text{yr}^{-1}$ . The predictions diverge more at higher SFRs, with the highest and lowest SFRF predictions differing by more than 1 dex at  $\text{SFR} > 10^2 M_{\odot}\text{yr}^{-1}$ .

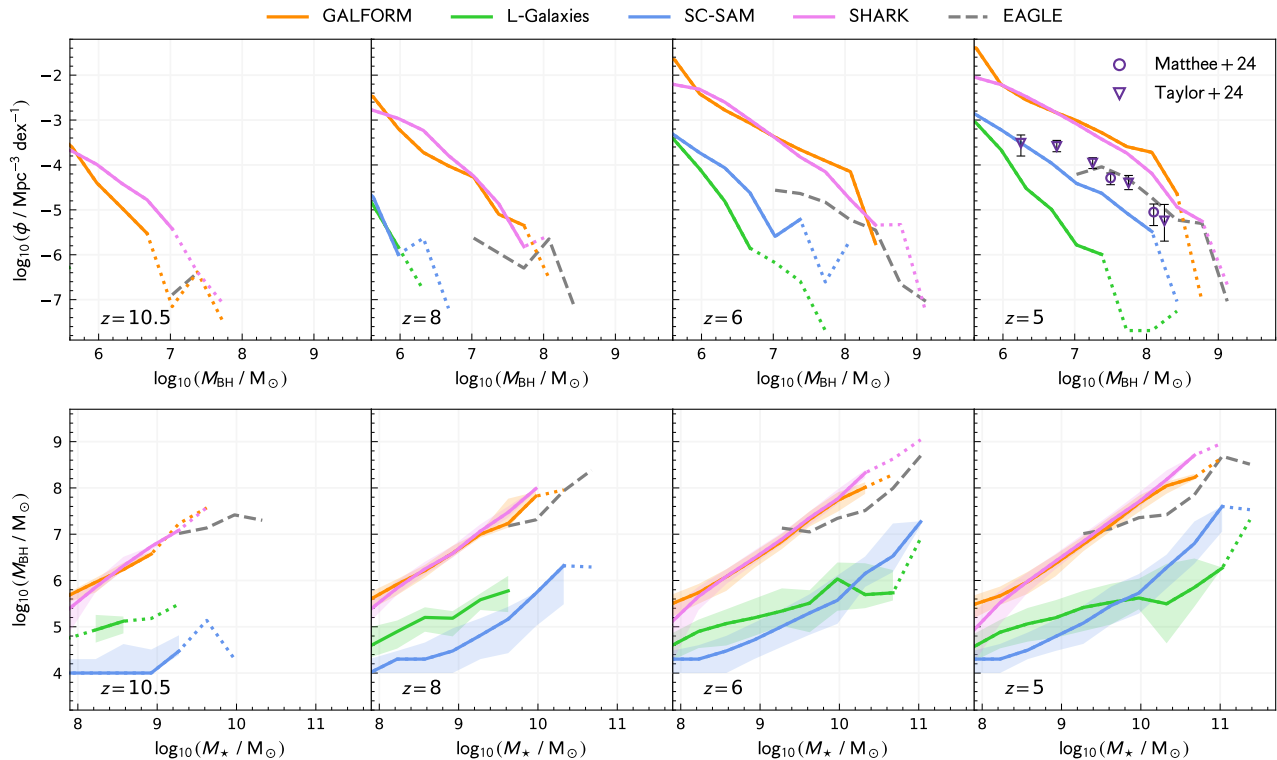


**Figure 4.** Each row shows a different quantity predicted by the four SAMs and EAGLE across a range of redshifts. The top row shows the black hole mass function, and the bottom row shows the stellar-to-black hole mass relation. Note that a black hole mass selection of  $M_{\text{BH}} > 10^7 M_{\odot}$  is applied to the EAGLE results, and that the EAGLE predictions at  $z = 10.5$  are at  $z = 10$ , as outputs of the fiducial FLARES suite are saved at integer redshift. For the SAMs, dotted lines denote bins containing fewer than 10 galaxies, and shaded regions denote the  $1\sigma$  range.

EAGLE and L-GALAXIES tend to predict the fewest galaxies at high SFRs ( $\text{SFR} > 10 M_{\odot} \text{Gyr}^{-1}$ ). This aligns with our previous observation of L-GALAXIES having a more gently-sloped SHMR, which is indicative of lower SFRs. However, it is interesting that EAGLE should predict few galaxies with high SFRs, given that the EAGLE SMF tends to be higher than that of L-GALAXIES and SHARK, and comparable to GALFORM at the high-mass end. Both GALFORM and SC-SAM predict larger populations of star-forming galaxies than the rest of the models at  $\text{SFR} > 10 M_{\odot} \text{Gyr}^{-1}$ . These are also the two models that have higher SMFs at  $M_{\star} > 10^9 M_{\odot}$ . At lower SFRs ( $\text{SFR} < 10^{1.5} M_{\odot} \text{Gyr}^{-1}$ ), SC-SAM tends to predict higher abundances, while EAGLE predicts the lowest abundances (note though that a stellar mass cut of  $M_{\star} > 10^8 M_{\odot}$  is applied to the EAGLE galaxies, thus the sample is incomplete at  $\text{SFR} < 1 M_{\odot} \text{Gyr}^{-1}$ ). Also shown are SFRFs estimated from *JWST* observations. Covelo-Paz et al. (2025) obtain SFR values by converting from  $H\alpha$  luminosities, and D’Silva et al. (2025) do so by fitting SEDs to photometry. The estimated SFRFs favour models with high number counts at  $\text{SFR} < 10 M_{\odot} \text{Gyr}^{-1}$ , and a subsequent steep decline, such as SHARK. We note that the estimated SFRs likely have large uncertainties than portrayed due to uncertainties in dust modelling and SED fitting.

The final row of Figure 3 shows the sSFR as a function of stellar mass. Across the SAMs, there is a gradual decrease in the sSFR with redshift, for fixed stellar mass. The model predictions are generally comparable. Interestingly, we find that GALFORM galaxies are slightly more star-forming than the other SAMs at  $z = 5 - 6$ , despite the GALFORM SMF being consistently lower than that of SC-SAM. This may be due to GALFORM adopting a top heavy initial mass

function (IMF), which leads to a larger fraction of stellar mass being instantaneously returned to the ISM when modelling starbursts (Lacey et al. 2016). This would also explain why, when looking at the SFRF, GALFORM produces more highly star-forming galaxies than SC-SAM. In L-GALAXIES, the median sSFR increases by  $\sim 0.5$  dex between  $\log_{10}(M_{\star}/M_{\odot}) = 7.5 - 10$ , while the other SAMs predict a flatter trend. In the appendix, we show the star-forming main sequence (SFS) predicted by the models, alongside several observations. The predicted relations are generally in good agreement with the observations, despite the differences seen here in Figure 3.

#### 4.4 Black hole properties

The SAMs predict vastly different black hole mass functions (BHMFs), with a difference of 2 – 3 dex between the highest and lowest predictions, as shown in the first row of Figure 4. GALFORM and SHARK predict the highest number of SMBHs across the mass range shown, and EAGLE predicts  $\sim 1$  dex fewer SMBHs with masses  $M_{\text{BH}} > 10^7 M_{\odot}$ . At lower masses,  $M_{\text{BH}} \sim 10^6 M_{\odot}$ , L-GALAXIES and SC-SAM predict number densities that are  $\sim 2$  dex lower than GALFORM and SHARK. The L-GALAXIES BHMF has a steeper negative slope than that of SC-SAM, due to a combination of L-GALAXIES predicting fewer galaxies at  $M_{\star} > 10^8 M_{\odot}$ , and also predicting lower mass black holes at a given stellar mass.

The second row of Figure 4 shows the black hole mass as a function of stellar mass. GALFORM and SHARK exhibit similar stellar-to-black hole mass ratios, despite having rather different black hole models. In L-GALAXIES, galaxies with a SMBH mass of  $M_{\text{BH}} > 10^6 M_{\odot}$

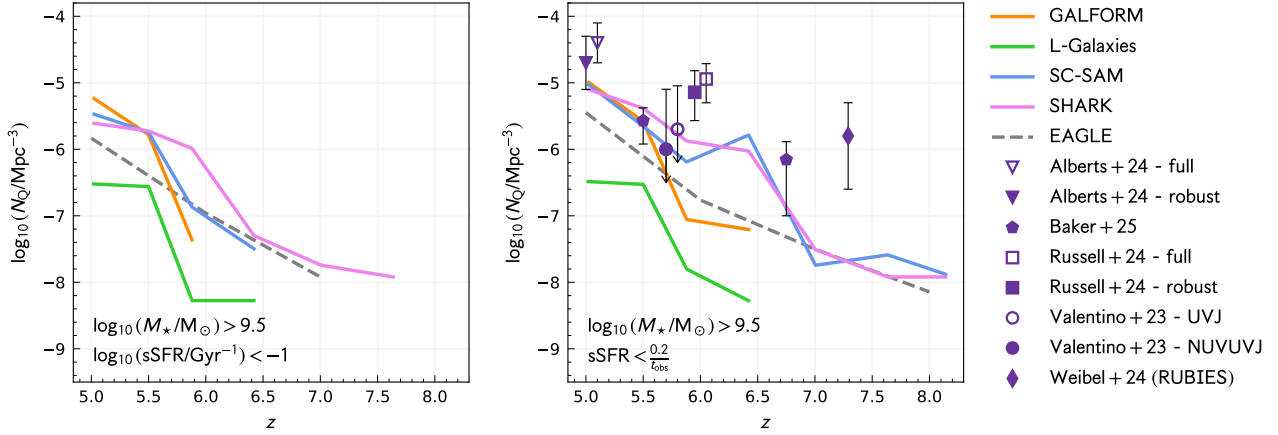


**Figure 5.** Number density of passive galaxies predicted by the four SAMs and EAGLE when run on the FLARES suite. In the left panel, the passive galaxy population is obtained using an sSFR cut of  $\log_{10}(\text{sSFR}/\text{Gyr}^{-1}) < -1$ . For a more appropriate comparison with observations, the right panel uses an sSFR cut of  $\log_{10}(\text{sSFR}/\text{Gyr}^{-1}) < 0.2/t_{\text{obs}}$ . A mass cut of  $\log_{10}(M_{\star}/M_{\odot}) > 9.5$  is applied to facilitate comparison with observations.

tend to have higher stellar masses than the other models. This could be in part due to the fact that black holes in the Yates et al. (2024) and Henriques et al. (2020) L-GALAXIES models do not grow through disk instabilities, which are known to contribute significantly to black hole growth in other versions of L-GALAXIES (Izquierdo-Villalba et al. 2020). Yung et al. (2021) mention that disk instabilities are an important mode of black hole growth in SC-SAM at early times (see also Hirschmann et al. 2012), and the same point is made by Lacey et al. (2016) regarding the GALFORM model.

We compare the predicted BHMFs at  $z = 5$  with observations by Matthee et al. (2024) and Taylor et al. (2024). Both studies identify broad H $\alpha$  emitters (HAEs), and assume them to be broad-line AGN (BLAGN). The BHMFs of SC-SAM and EAGLE roughly agree with these observations. However, as BLAGN are a subset of the total black hole population, the observations serve as lower limits rather than an estimate of the actual BHMF. The predictions by GALFORM and SHARK may thus be closer to the truth.

## 5 QUIESCENT GALAXIES

In this section, we study the characteristics of quiescent galaxies predicted by the models. For the most part, we adopt the following definition of passivity:

$$\log_{10}(\text{sSFR}/\text{Gyr}^{-1}) < -1. \quad (1)$$

We explored using a selection based on distance from the SFS, and found that for a difference of 1.5 dex, the results obtained are similar. In §5.1, we also use an alternative, time-dependent definition:

$$\text{sSFR} < \frac{0.2}{t_{\text{obs}}}, \quad (2)$$

where  $t_{\text{obs}}$  is the age of the universe at the observed redshift of the galaxy (Pacifci et al. 2016). This definition is more commonly used amongst observers.

### 5.1 Number density

Figure 5 shows the number density of massive quiescent galaxies as a function of redshift for two definitions of passivity, given by

Equations 1 and 2 (left and right panels, respectively). Observations are also plotted, although the comparison is not quite apples-to-apples, given systematics such as the SFR timescale, and inherent differences in how simulated and observed galaxies are identified. Still, Equation 2 allows for a more appropriate comparison with recent observational estimates from JWST:

- Albers et al. (2024) use NIRCcam and MIRI data from the JADES field in their analysis. They select their full sample by UVJ classification (Antwi-Danso et al. 2023), and identify robust passive candidates by requiring that 97.5% of a galaxy’s sSFR posterior, obtained from SED-fitting with BAGPIPES (Carnall et al. 2018), satisfies Equation 2. Their number densities are reported for stellar masses  $\log_{10}(M_{\star}/M_{\odot}) > 9.5$ .

- Baker et al. (2025) identify passive galaxies by analysing NIRCcam imaging from multiple JWST fields. A preliminary sample is identified using a relaxed UVJ selection, and processed using the BAGPIPES SED-fitting code. Galaxies with sSFRs that satisfy Equation 2 are considered to be passive. We show their predictions for galaxies with stellar masses  $\log_{10}(M_{\star}/M_{\odot}) > 9.5$ .

- Russell et al. (2024) identify passive galaxies in the NEP, CEERS and JADES fields using primarily NIRCcam imaging. They make their selection following Equation 2 – at least 50% (97.5%) of a galaxy’s sSFR posterior must meet the sSFR criteria to be included in the full (robust) sample. We show their estimated number densities for galaxies in the stellar mass range  $\log_{10}(M_{\star}/M_{\odot}) > 9.5$  by summing the number densities obtained for their two highest stellar mass bins.

- Valentino et al. (2023) analyse NIRCcam, NIRISS and MIRI data from 11 JWST fields in their search for passive galaxies. Two selections are made, the first in relaxed UVJ space, and the second using Gaussian mixture modelling to identify candidates in NUV–U, U–V, V–J space. Their predictions are shown for the stellar mass range  $\log_{10}(M_{\star}/M_{\odot}) > 9.5$ .

- Weibel et al. (2024a) provide an estimate of the passive galaxy number density based on the discovery of RUBIES-UDS-QG-z7, a passive galaxy in the UltraDeep Survey (UDS) field, assuming a survey volume of  $\sim 300 \text{ arcmin}^{-2}$  (PRIMER-UDS and CEERS combined).

Comparing both panels of Figure 5, we find that the fixed cut-off

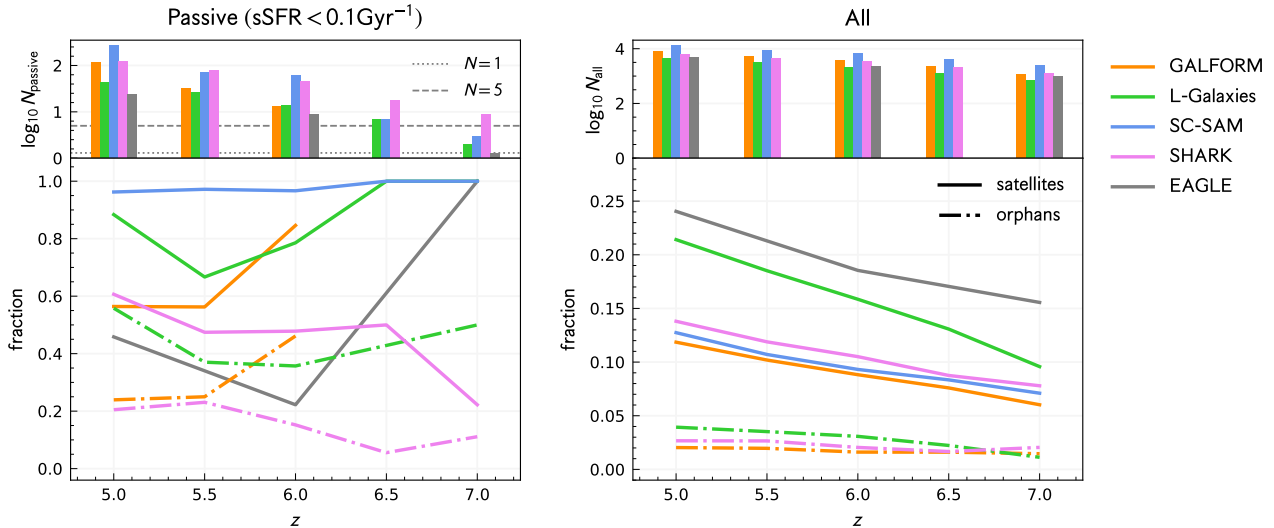


**Figure 6.** The left and right plots show the same statistics for different galaxy populations – the passive galaxy population ( $\log_{10}(M_{\star}/M_{\odot}) > 9$  and  $\log_{10}(\text{sSFR}/\text{Gyr}^{-1}) < -1$ ) on the left, and the general galaxy population ( $\log_{10}(M_{\star}/M_{\odot}) > 9$ ) on the right. The top panels show, for each population, the raw counts of galaxies predicted by the four SAMs and EAGLE, as a function of redshift. The dotted and dashed grey lines in the top left panel indicate the height of a bin containing 1 and 5 galaxies respectively. Note that bins containing one galaxy are displayed as slightly larger than one, so that they appear on the plot. The bottom panels show the fraction of satellites and orphans (a subset of satellites), represented by solid and dot-dashed lines respectively. The orphan class of galaxies is applicable to neither SC-SAM nor EAGLE – in SC-SAM, satellites are modelled analytically, and EAGLE is a hydrodynamics model. No information is shown for the EAGLE run at  $z = 5.5$  and  $6.5$ , as fiducial FLARES snapshots are saved at integer redshifts only.

described by Equation 1 results in slightly lower number densities predicted by the models compared to the time-dependent cut-off described by Equation 2, which is more relaxed at higher redshifts. In general, the passive abundances predicted by GALFORM, SC-SAM and SHARK are comparable at  $z = 5$ , but the GALFORM distribution function drops off more quickly as redshift increases. L-GALAXIES predicts the fewest passive galaxies,  $\sim 1-2$  dex below SC-SAM and SHARK at  $z = 5-6$ . Note that the EAGLE passive galaxies studied in this paper are not necessarily the same as those in Lovell et al. (2023b), due to the differing physical apertures (and timescales, in the case of SFRs) over which galaxy properties are averaged.

Observations shown in the right panel of Figure 5 favour the higher passive abundances predicted by SC-SAM and SHARK. None of the models in our analysis predict the abundance estimated by Weibel et al. (2024a) – reproducing this has been a struggle for most models in general, although the COLIBRE simulation is one exception (Chaikin et al. 2025; Schaye et al. 2025, Chandro-Gomez et al. *in prep*). L-GALAXIES appears to consistently underestimate the number density of passive galaxies at  $z \geq 5$ . Araya-Araya et al. (2025), who explore different calibrations of L-GALAXIES, also find a similar result at high redshift. More observations will help to clarify the effect of cosmic variance on these observational estimates – studies have shown that the size and depth of a survey may play a large role in the scatter of observed passive abundances (Thomas et al. 2023; Valentino et al. 2023; Jespersen et al. 2025). This seems to be the case at lower redshifts ( $3 < z < 5$ ), where passive abundances can vary by more than 1 dex from study to study (Carnall et al. 2023; Gould et al. 2023; Valentino et al. 2023; Alberts et al. 2024; Russell et al. 2024).

## 5.2 Satellite fractions

To investigate the nature of these passive galaxies, we first look at the proportion of centrals and satellite galaxies in the passive galaxy population. Generally, passive satellites are thought to be quenched more by environmental processes, and passive centrals more by AGN feedback. As we will see in the next section (§5.3), this distinction is valid for the SAMs, with the exception that AGN feedback in L-GALAXIES and SC-SAM is not effective at the redshifts probed in this paper, perhaps due to SMBHs not growing quickly enough at high redshift (see Figure 4). In EAGLE, it turns out that AGN feedback is the primary driver of passivity (also discussed in §5.3). From here on, a slightly lower stellar mass threshold of  $\log_{10}(M_{\star}/M_{\odot}) > 9$  is used, as we are no longer comparing with observations, but still focused on the massive galaxy population.

Figure 6 shows that for all models in this analysis, across the redshifts probed, we find higher fractions of satellites in the passive galaxy population compared to the general galaxy population. This is particularly the case for the SAMs. At  $z = 5$ ,  $> 55\%$  of the passive galaxy population predicted by the SAMs are satellites, in contrast to  $< 25\%$  of the general galaxy population. L-GALAXIES and SC-SAM predict notably high satellite fractions ( $> 90\%$  at  $z = 5$ ). Similar trends are observed at higher redshifts, though we caution that the statistics are less robust as redshift increases. Compared to the SAMs, EAGLE predicts a smaller contrast, with satellites making up 45% of the passive population and 25% of the general population at  $z = 5$ .

Satellites in SAMs are modelled in a highly idealised manner, which may lead to more rapid quenching, and thus higher passive fractions. For example, all satellites in GALFORM and SC-SAM are instantaneously stripped of hot gas, such that none can cool and form stars, whereas gradual hot gas stripping is applied in L-GALAXIES and SHARK. In reality, galaxies should be able to retain their hot halo for a period of time after becoming a satellite. Guo et al. (2016) find that adopting a gradual stripping of hot gas in GALFORM leads to

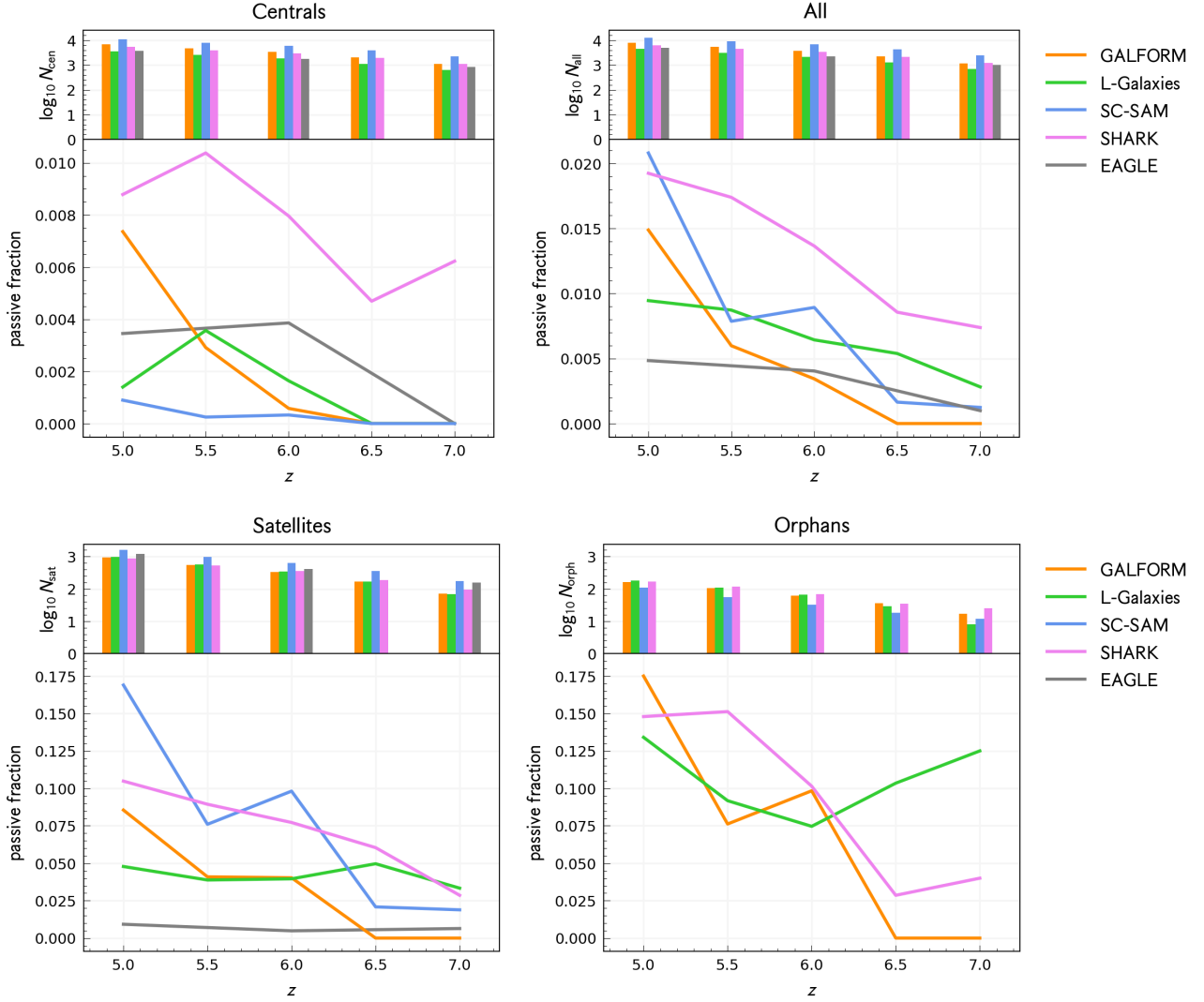


**Figure 7.** Each of the four subplots shows the same statistics for different galaxy populations (clockwise, from the top left): centrals, all galaxies, satellites, and orphans (a subset of satellites). A stellar mass cut of  $\log_{10}(M_{\star}/M_{\odot}) > 9$  is applied in all cases. The top panel of each subplot shows, for the galaxy population, the raw counts of galaxies predicted by the four SAMs and EAGLE, as a function of redshift. The bottom panel shows the fraction of the population that are passive, i.e. with  $\log_{10}(\text{sSFR}/\text{Gyr}^{-1}) < -1$  at a given redshift. No information is shown for the EAGLE run at  $z = 5.5$  and  $6.5$ , as fiducial FLARES snapshots are saved at integer redshift only.

passive satellite numbers in closer agreement with EAGLE. It is also possible for gas stripping to be overly strong in the SAMs that do not implement it instantaneously – Harrold et al. (2024) suggest that the discrepancy between the predicted and observed number of low-mass ( $9 < \log_{10}(M_{\star}/M_{\odot}) < 10$ ) passive galaxies in L-GALAXIES at  $z < 3$  could be solved if orphan galaxies were allowed to retain a larger cold gas supply.

Having noted a tendency for passive galaxies to be satellites rather than centrals, we can ask the question of how likely it is that a galaxy is passive, if it is a central, satellite or orphan. Figure 7 shows the passive fractions of the various galaxy populations. At  $z = 5$ , EAGLE predicts the lowest passive fraction overall (0.5%), and the SAMs predict passive fractions between 1 – 2%. For all models, we find higher passive fractions in the satellite population compared to the central galaxy population, at a given redshift. In the SAMs, this suggests that the satellite-related processes are more effective at quenching

galaxies than AGN. As mentioned in the opening paragraph of this section, this is less obviously the case in the EAGLE model.

Passive fractions do not exceed 20% for the satellite populations, indicating that it is still a relatively small subset of satellites that are quenched. Focusing on satellites, we see that EAGLE predicts the lowest passive fraction at  $z = 5$  (1%), while SC-SAM predicts the highest (17%), suggesting that the adopted satellite prescription is highly conducive to quenching. SHARK, GALFORM and L-GALAXIES fall in between, with passive fractions of  $\sim 10\%$ ,  $8\%$  and  $5\%$  in their satellite populations respectively. When it comes to the population of centrals at  $z = 5$ , it is L-GALAXIES and SC-SAM with the lowest passive fractions ( $\sim 0.1\%$ ), GALFORM and SHARK with highest passive fractions ( $\sim 0.8\%$ ), and EAGLE in between (0.35%). SHARK has a central galaxy passive fraction consistently higher than the rest ( $> 0.5\%$ ) at  $z = 5 - 7$ , which suggests that AGN feedback is a particularly strong driver of passivity and effective out to higher redshifts, compared to the other models.

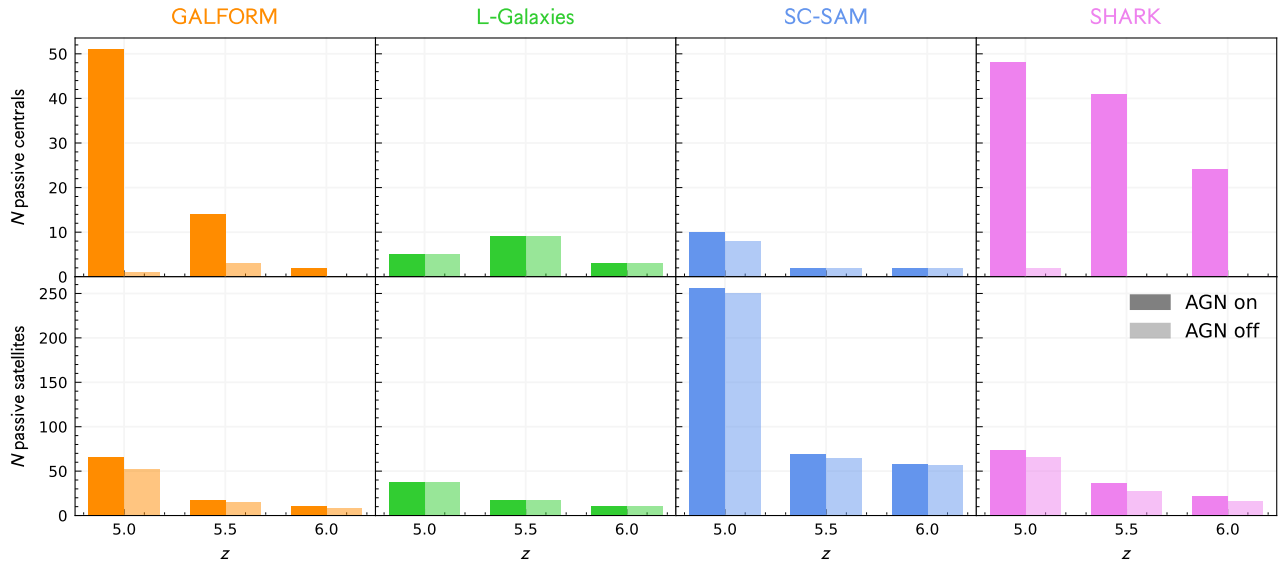


**Figure 8.** The top (bottom) row shows, the raw number count of central (satellite) galaxies that are passive when AGN feedback is left on (solid bars) or turned off (translucent bars), as a function of redshift. Each column shows the data for a different SAM, from left to right, GALFORM, L-GALAXIES, SC-SAM and SHARK. Passivity is defined using the sSFR cut  $\log_{10}(\text{sSFR}/\text{Gyr}^{-1}) < -1$ . A stellar mass cut of  $\log_{10}(M_{\star}/M_{\odot}) > 9$  is applied as well.

### 5.3 Quenching mechanisms

In the previous section (§5.2), we looked at the occurrence of passivity in central and satellite galaxies, with the idea that passivity in these two populations may be caused by different physical processes. In this section, we explore quenching pathways in more detail. Due to the fundamental differences between hydrodynamic and semi-analytic models, we consider the two types of models separately.

#### 5.3.1 Quenching in the EAGLE model

Passivity in the fiducial FLARES suite (which uses the EAGLE hydrodynamics model) has been studied in detail by Lovell et al. (2023b). Their main finding is that passivity is strongly driven by SMBH feedback, regardless of whether the galaxy is a satellite or central. When black holes in EAGLE accrete mass, an amount of energy proportional to the accretion rate is stored in a reservoir, to be used for AGN feedback. Once sufficient energy is available, feedback occurs via the stochastic heating of neighbouring gas particles. Lovell et al. (2023b) investigate the evolutionary histories of quiescent galaxies in the fiducial FLARES suite and find that all exhibit a rapid decrease in SFR alongside a sharp spike in SMBH accretion rate. Thus, Lovell et al. (2023b) suggest that a galaxy is quenched when strong SMBH accretion triggers a feedback event that heats up the ISM, preventing further star formation.

With this in mind, it is interesting that at  $z = 5$ , we observe quiescent galaxies in EAGLE to be slightly biased towards being satellite galaxies (see discussion in §5.2, and Figures 6 and 7). As EAGLE is a hydrodynamics model, there are no direct restrictions on the gas available for AGN in satellites to accrete. Thus, satellites are able to retain some hot gas that is then accreted onto the SMBH, allowing the transition from central to satellite occur smoothly, with no changes to the physics modelling. It is important to mention that we are limited by low number statistics – at  $z = 5$ , the EAGLE model predicts a total of 24 passive galaxies in FLARES (defined by  $\log_{10}(M_{\star}/M_{\odot}) > 9$  and  $\log_{10}(\text{sSFR}/\text{Gyr}^{-1}) < -1$ ). If the bias is indeed a feature of the model, a study by Visser-Zadovnyi et al. (2025) on the quenching

timescale of  $z = 0$  satellite galaxies in EAGLE could provide some insight. By tracking gas particles, Visser-Zadovnyi et al. (2025) find that satellites and centrals are similarly subject to outflows, likely from stellar or AGN feedback (Mitchell et al. 2020). Crucially, while central galaxies are continuously replenished by inflows of fresh gas, satellites are not, and eventually run out of star-forming gas. It may be that a similar scenario is occurring in the fiducial FLARES suite at high-redshift, contributing to the higher fraction of satellites in the passive galaxy population. This is speculative – at higher redshifts, we would expect increased gas accretion rates onto galaxies due to increased accretion rates onto halos (van de Voort et al. 2017), and so cannot confidently assume that the ‘starvation’ of satellites is occurring. Regardless of the role played by environmental processes, Lovell et al. (2023b) show that passive galaxies do not form when AGN feedback is turned off, which strongly suggests that AGN feedback is the dominant quenching mechanism in EAGLE at  $z > 5$ .

#### 5.3.2 Quenching in SAMs

SAMs are, by definition, more prescriptive than hydrodynamic simulations. AGN feedback and environmental effects are generally understood to cause passivity in centrals and satellites respectively, at least at low redshift. Here, we test this hypothesis at high redshift.

To evaluate the impact of AGN feedback on passivity, we rerun the SAMs with AGN feedback turned off<sup>4</sup> and examine how the number of passive satellites and centrals changes. Our results are summarised in Figure 8. When AGN feedback is turned off, the number of passive centrals predicted by GALFORM and SHARK is reduced to zero, or close to zero. This suggests that in the two models, AGN feedback is the primary driver of passivity in central galaxies. Turning off AGN feedback makes little or no difference to the number of passive centrals predicted by L-GALAXIES and SC-SAM, suggesting

<sup>4</sup> Where models implement more than one mode of AGN feedback, all modes are turned off.

that central galaxies are not quenched by AGN feedback at these redshifts. We note that both models predict relatively few passive centrals ( $< 10$ ) compared to GALFORM and SHARK ( $\sim 50$  at  $z = 5$ ). Our finding for SC-SAM agrees with that of Yung et al. (2019a), who observe no difference in their  $z > 4$  analysis when turning off AGN feedback. Henriques et al. (2017) mention AGN feedback as a cause of passivity in L-GALAXIES at low-redshift, but it seems that it is not yet effective at high-redshift, perhaps due to the slow growth rate of SMBHs, as observed in Figure 4 (and discussed in §4.4).

In the SAMs, the impact of AGN feedback on satellite galaxies is minimal. Having seen that AGN feedback has little effect on the number of passive centrals predicted by L-GALAXIES and SC-SAM, it is not surprising that we should observe the same trend for passive satellites in these two models. In GALFORM, satellite galaxies do not undergo AGN feedback, as they do not retain their hot halo (a prerequisite for AGN feedback). The small reduction in the number of passive satellites when AGN feedback is turned off may be attributed to the effects of AGN feedback prior to the transition from central to satellite. In SHARK, AGN feedback continues as per normal in satellite galaxies (provided the necessary conditions are met), however, the similar numbers of passive satellites observed in runs with and without AGN feedback show that AGN feedback is not a primary quenching mechanism of satellites in SHARK.

The link between passivity and satellite-related processes in SAMs is well-established – it has been mentioned and explored in previous works, e.g. Guo et al. (2016) for GALFORM, Guo et al. (2011); Harrold et al. (2024); Vani et al. (2025) for L-GALAXIES, Somerville et al. (2008); Porter et al. (2014) for SC-SAM, Lagos et al. (2025) for SHARK. While the exact treatment of satellites differs between the models, all prescriptions essentially reduce the amount of cold gas available for forming stars by stripping away hot gas (which would cool into cold gas), and in some cases by stripping away cold gas as well. All the SAMs in this analysis have  $H_2$ -dependent SFRs. Thus, the SFR of a galaxy tends to trace its cold gas mass. In Section C of the Appendix, we include a plot of the evolutionary histories of several passive galaxies predicted by the SAMs, which highlights how the cold gas mass and sSFR decrease in tandem when a galaxy becomes a satellite.

Our findings suggest that the vast majority of passive satellites in the SAMs are indeed quenched by satellite-related processes. AGN feedback appears to play a significant role in the quenching of centrals in GALFORM and SHARK, but not in L-GALAXIES and SC-SAM.

#### 5.4 Discussion

We have built up a general picture of AGN feedback being the main driver of passivity in EAGLE, and environmental quenching being more prevalent in the SAMs. In EAGLE, AGN feedback leads to outflows of gas in both centrals and satellites alike. It is possible that satellites in EAGLE are additionally quenched by a lack of fresh gas, as inflows tend to draw towards central galaxies (Visser-Zadovornyi et al. 2025). This is quite different from what we see in the SAMs, where AGN feedback can drive passivity in centrals (in the case of GALFORM and SHARK), but contributes minimally to the quenching of satellites. In the SAMs, passivity in satellites is mainly attributed to environmental processes such as ram pressure stripping and tidal stripping. While passive galaxies have been observed at high-redshift, not much information is available as to how they are quenched, or whether they are centrals or satellites. At lower redshift ( $1.5 < z < 3$ ), there is some evidence that L-GALAXIES tends to over-predict the number of low-mass ( $9 < \log_{10}(M_*/M_\odot) < 10$ ) passive galaxies (Asquith et al. 2018; Harrold et al. 2024) and under-

predict the number of high-mass ( $\log_{10}(M_*/M_\odot) > 10.5$ ) passive galaxies (Henriques et al. 2020; Vani et al. 2025), which suggests that environmental quenching may be overly strong and AGN feedback not strong enough. Figure 5 showed that the SAMs predict passive galaxy abundances that are either in line with or lower than observational estimates. Thus, if any of the SAMs, particularly those with high satellite fractions in their passive populations, do predict too many environmentally-quenched satellites at  $z > 5$ , then quenching by AGN feedback would have to occur more frequently to match the observed passive abundances. In EAGLE, satellite evolution is already self-consistently modelled. Hence, the modelling of AGN would have to be adjusted to better match high-redshift observations (Turner et al. 2025).

## 6 CONCLUSIONS

We have run four SAMs (GALFORM, L-GALAXIES, SC-SAM and SHARK) at  $5 \leq z \leq 12$  using the FLARES simulation strategy. The predictions of the SAMs are compared with recent observations from JWST, as well as results from the fiducial FLARES suite, which is run with the EAGLE hydrodynamics model. In this paper, we have explored the general properties of the simulated galaxies and also taken a closer look at how passive galaxies form in the different models. Our results are summarised below:

- At  $z < 10$ , there is generally good overlap between the predicted SMFs and recent observational estimates. SC-SAM predicts the highest abundances at  $\log_{10}(M_*/M_\odot) > 9$ , and L-GALAXIES tends to predict fewer galaxies, especially at the highest masses ( $\log_{10}(M_*/M_\odot) > 10$ ). At  $z > 10$ , the models tend to under-predict the SMF relative to observations, however we caution that observations are more uncertain at such early times.
- Looking at the SHMR, we find that central galaxies in low-mass ( $\log_{10}(M_{\text{halo}}/M_\odot) < 10$ ) halos are most massive in L-GALAXIES, but grow more slowly compared to the other three SAMs. On the other hand, GALFORM has the steepest SHMR, predicting the smallest galaxies in  $M_{\text{halo}} < 10^{10} M_\odot$  halos and catching up to the other models at higher masses.
- The sSFRs predicted by the models are generally comparable. Galaxies in GALFORM tend to be the most highly star-forming despite the model not predicting the highest SMF – this could be due to the top heavy IMF adopted. In GALFORM, SC-SAM and SHARK, the sSFR of galaxies remains roughly constant at  $\log_{10}(M_*/M_\odot) > 8$ , while in L-GALAXIES, the sSFR appears to increase with stellar mass. Looking at the SFRF, we find that L-GALAXIES predicts the fewest highly star-forming galaxies ( $\text{SFR} > 10 M_\odot \text{yr}^{-1}$ ), while GALFORM and SC-SAM tend to predict the most.
- There are significant differences in the black hole populations predicted by the different models, with GALFORM and SHARK predicting the highest number densities, and L-GALAXIES and SC-SAM predicting number densities  $\geq 2$  dex lower. The EAGLE BHMF is somewhere in the middle, closest to observational estimates. However, we note that the observations likely underestimate the total black hole abundances. In agreement with our findings on the BHMF, we note that GALFORM and SHARK predict higher black hole masses for a galaxy of a given stellar mass than L-GALAXIES and SC-SAM.
- In terms of passive number densities, the model predictions are at the low end of observational constraints. We find a wide range of predictions, with SC-SAM and SHARK generally predicting the highest passive abundances, but for different reasons (see below).
- The majority of the passive galaxies at  $\log_{10}(M_*/M_\odot) > 9$  in EAGLE are centrals. Previous analysis by Lovell et al. (2023b)

of the fiducial FLARES suite identifies AGN feedback as the main driver of passivity, be it in centrals or satellites. We find that the fraction of satellites in the passive population is still slightly higher than the fraction of satellites in the general galaxy population. This might be explained by the contribution of additional environmental effects such as satellites being starved of gas (Visser-Zadvornyi et al. 2025), however, due to low number counts we are tentative with this suggestion.

- We show that passive satellites in the SAMs are primarily quenched by environmental processes. Passive centrals in GALFORM and SHARK are likely caused by AGN feedback, while in L-GALAXIES and SC-SAM, we find that AGN feedback is not yet an effective quenching mechanism. Passive galaxies in SC-SAM are especially biased towards being satellites, with a satellite fraction of > 90%.

In this study, we find model predictions of the SMF and SFRF to be generally within range of high-redshift observations. More discrepancy is observed in the BHMF and passive galaxy abundances. Our findings highlight how differences in the modelling of satellite galaxies and black holes affect the predicted properties of passive galaxies. An in-depth exploration of the physics modelling was not within the scope of this paper, but would certainly be an interesting and feasible topic for future studies, given the resource-friendly nature of SAMs and the FLARES zoom strategy.

## ACKNOWLEDGEMENTS

We wish to thank the EAGLE team for their efforts in developing the EAGLE simulation code, as well as Scott Kay and Adrian Jenkins for their invaluable help getting up and running with the EAGLE resimulation code. We also very grateful to John Helly for his advice with running GALFORM, and for allowing us to use the DHALO code.

This work used the DiRAC@Durham facility managed by the Institute for Computational Cosmology on behalf of the STFC DiRAC HPC Facility ([www.dirac.ac.uk](http://www.dirac.ac.uk)). The equipment was funded by BEIS capital funding via STFC capital grants ST/K00042X/1, ST/P002293/1, ST/R002371/1 and ST/S002502/1, Durham University and STFC operations grant ST/R000832/1. DiRAC is part of the National e-Infrastructure. Additionally, we have had the assistance of resources from the National Computational Infrastructure (NCI Australia), an NCRIS enabled capability supported by the Australian Government. We wish to acknowledge the following open source software packages used in the analysis: MATPLOTLIB (Hunter 2007), NUMPY (Harris et al. 2020).

LTCS, MGAM and JCT are supported by STFC studentships. CMB and CGL acknowledge support from the STFC through ST/X001075/1. The Flatiron Institute is supported by the Simons Foundation. WJR, APV and SMW acknowledge support from the Sussex Astronomy Centre STFC Consolidated Grant ST/X001040/1. CP acknowledges the support of the ARC Centre of Excellence for All Sky Astrophysics in 3 Dimensions (ASTRO 3D), through project number CE170100013.

The ordering of the author list was decided as follows: 1) main author, 2) authors who were highly involved in running the SAMs or helping the main author to do so (in alphabetical order), 3) remaining authors. We list here the roles and contributions of the authors according to the Contributor Roles Taxonomy (CRediT)<sup>5</sup>. **Louise T. C. Seeyave**: Conceptualization, Data curation, Methodology, Investigation, Formal Analysis, Visualization, Writing - original

draft. **Stephen M. Wilkins**: Conceptualization, Methodology, Writing - review & editing. **Christopher C. Lovell**, **Aswin P. Vijayan**: Data curation, Methodology, Writing - review & editing. **Carlton M. Baugh**, **Ángel Chandro-Gómez**, **Claudia del P. Lagos**, **Chris Power**, **Rachel S. Somerville**, **Robert M. Yates**, **L. Y. Aaron Yung**: Data curation, Writing - review & editing. **Cedric G. Lacey**, **Shihong Liao**, **Maxwell A.G. Maltz**, **William J. Roper**, **Jack C. Turner**: Writing - review & editing.

## DATA AVAILABILITY

Data is available on request from the corresponding author. Plots from the convergence tests may be found in the corresponding author's thesis, which will be publicly available shortly.

## REFERENCES

- Adams N. J., et al., 2024, *ApJ*, **965**, 169  
 Alberts S., et al., 2024, *ApJ*, **975**, 85  
 Antwi-Danso J., et al., 2023, *ApJ*, **943**, 166  
 Araya-Araya P., Cochrane R. K., Hayward C. C., Sodré Jr. L., Yates R. M., van Daalen M. P., Vicentin M. C., 2025, *MNRAS*, **542**, 2808  
 Asquith R., et al., 2018, *MNRAS*, **480**, 1197  
 Ayromlou M., Nelson D., Yates R. M., Kauffmann G., Renneby M., White S. D. M., 2021, *MNRAS*, **502**, 1051  
 Baker W. M., et al., 2025, *arXiv e-prints*, p. [arXiv:2506.04119](https://arxiv.org/abs/2506.04119)  
 Barnes D. J., Kay S. T., Henson M. A., McCarthy I. G., Schaye J., Jenkins A., 2017a, *MNRAS*, **465**, 213  
 Barnes D. J., et al., 2017b, *MNRAS*, **471**, 1088  
 Baugh C. M., Cole S., Frenk C. S., 1996, *MNRAS*, **283**, 1361  
 Baugh C. M., et al., 2019, *MNRAS*, **483**, 4922  
 Behroozi P. S., Wechsler R. H., Wu H.-Y., 2013a, *ApJ*, **762**, 109  
 Behroozi P. S., Wechsler R. H., Wu H.-Y., Busha M. T., Klypin A. A., Primack J. R., 2013b, *ApJ*, **763**, 18  
 Benson A. J., 2010, *Phys. Rep.*, **495**, 33  
 Binney J., Tremaine S., 1987, Galactic dynamics  
 Blitz L., Rosolowsky E., 2006, *ApJ*, **650**, 933  
 Bondi H., Hoyle F., 1944, *MNRAS*, **104**, 273  
 Bower R. G., Benson A. J., Malbon R., Helly J. C., Frenk C. S., Baugh C. M., Cole S., Lacey C. G., 2006, *MNRAS*, **370**, 645  
 Boylan-Kolchin M., Ma C.-P., Quataert E., 2008, *MNRAS*, **383**, 93  
 Boylan-Kolchin M., Springel V., White S. D. M., Jenkins A., Lemson G., 2009, *MNRAS*, **398**, 1150  
 Bryan G. L., Norman M. L., 1998, *ApJ*, **495**, 80  
 Carnall A. C., McLure R. J., Dunlop J. S., Davé R., 2018, *MNRAS*, **480**, 4379  
 Carnall A. C., et al., 2023, *MNRAS*, **520**, 3974  
 Castellano M., et al., 2023, *ApJ*, **948**, L14  
 Chabrier G., 2003, *PASP*, **115**, 763  
 Chaikin E., et al., 2025, *arXiv e-prints*, p. [arXiv:2509.07960](https://arxiv.org/abs/2509.07960)  
 Chandro-Gómez Á., et al., 2025, *MNRAS*, **539**, 776  
 Chiang Y.-K., Overzier R., Gebhardt K., 2013, *ApJ*, **779**, 127  
 Clarke L., Shapley A. E., Sanders R. L., Topping M. W., Brammer G. B., Bento T., Reddy N. A., Kehoe E., 2024, *ApJ*, **977**, 133  
 Cole S., Lacey C. G., Baugh C. M., Frenk C. S., 2000, *MNRAS*, **319**, 168  
 Correa C. A., Schaye J., van de Voort F., Duffy A. R., Wyithe J. S. B., 2018, *MNRAS*, **478**, 255  
 Covelo-Paz A., et al., 2025, *A&A*, **694**, A178  
 Cowley W. I., Baugh C. M., Cole S., Frenk C. S., Lacey C. G., 2018, *MNRAS*, **474**, 2352  
 Crain R. A., et al., 2015, *MNRAS*, **450**, 1937  
 Croton D. J., et al., 2006, *MNRAS*, **365**, 11  
 Croton D. J., et al., 2016, *ApJS*, **222**, 22  
 Cueto E. R., Hutter A., Dayal P., Gottlöber S., Heintz K. E., Mason C., Trebitsch M., Yepes G., 2024, *A&A*, **686**, A138

<sup>5</sup> <https://credit.niso.org/>

- Cui W., et al., 2018, *MNRAS*, 480, 2898
- D’Silva J. C. J., et al., 2025, *arXiv e-prints*, p. [arXiv:2503.03431](https://arxiv.org/abs/2503.03431)
- Davis M., Efstathiou G., Frenk C. S., White S. D. M., 1985, *ApJ*, 292, 371
- De Lucia G., Boylan-Kolchin M., Benson A. J., Fontanot F., Monaco P., 2010, *MNRAS*, 406, 1533
- Desprez G., et al., 2024, *MNRAS*, 530, 2935
- Di Matteo T., Springel V., Hernquist L., 2005, *Nature*, 433, 604
- Elahi P. J., Welker C., Power C., Lagos C. d. P., Robotham A. S. G., Cañas R., Poulton R., 2018, *MNRAS*, 475, 5338
- Elahi P. J., Poulton R. J. J., Tobar R. J., Cañas R., Lagos C. d. P., Power C., Robotham A. S. G., 2019, *Publ. Astron. Soc. Australia*, 36, e028
- Elmegreen B. G., 1993, *ApJ*, 411, 170
- Errani R., Penarrubia J., Tormen G., 2015, *MNRAS*, 449, L46
- Feldmann R., Mayer L., 2015, *MNRAS*, 446, 1939
- Ferland G. J., Korista K. T., Verner D. A., Ferguson J. W., Kingdon J. B., Verner E. M., 1998, *PASP*, 110, 761
- Finkelstein S. L., et al., 2023, *ApJ*, 946, L13
- Finkelstein S. L., et al., 2024, *ApJ*, 969, L2
- Font A. S., et al., 2008, *MNRAS*, 389, 1619
- Fu J., Guo Q., Kauffmann G., Krumholz M. R., 2010, *MNRAS*, 409, 515
- Fu J., et al., 2013, *MNRAS*, 434, 1531
- Gabrielpillai A., Somerville R. S., Genel S., Rodriguez-Gomez V., Pandya V., Yung L. Y. A., Hernquist L., 2022, *MNRAS*, 517, 6091
- Gardner J. P., et al., 2006, *Space Sci. Rev.*, 123, 485
- Gelli V., Mason C., Hayward C. C., 2024, *ApJ*, 975, 192
- Gnedin N. Y., Kravtsov A. V., 2011, *ApJ*, 728, 88
- Gómez J. S., Padilla N. D., Helly J. C., Lacey C. G., Baugh C. M., Lagos C. D. P., 2022, *MNRAS*, 510, 5500
- Gould K. M. L., et al., 2023, *AJ*, 165, 248
- Greene J. E., et al., 2024, *ApJ*, 964, 39
- Griffin A. J., Lacey C. G., Gonzalez-Perez V., Lagos C. d. P., Baugh C. M., Fanidakis N., 2019, *MNRAS*, 487, 198
- Griffin A. J., Lacey C. G., Gonzalez-Perez V., Lagos C. d. P., Baugh C. M., Fanidakis N., 2020, *MNRAS*, 492, 2535
- Guo Q., et al., 2011, *MNRAS*, 413, 101
- Guo Q., et al., 2016, *MNRAS*, 461, 3457
- Hadzhiyska B., Liu S., Somerville R. S., Gabrielpillai A., Bose S., Eisenstein D., Hernquist L., 2021, *MNRAS*, 508, 698
- Harikane Y., et al., 2023, *ApJ*, 959, 39
- Harris C. R., et al., 2020, *Nature*, 585, 357
- Harrold J. E., Almaini O., Pearce F. R., Yates R. M., 2024, *MNRAS*, 532, L61
- Harvey T., et al., 2024, *arXiv e-prints*, p. [arXiv:2403.03908](https://arxiv.org/abs/2403.03908)
- Henriques B. M. B., White S. D. M., Thomas P. A., Angulo R. E., Guo Q., Lemson G., Wang W., 2017, *MNRAS*, 469, 2626
- Henriques B. M. B., Yates R. M., Fu J., Guo Q., Kauffmann G., Srisawat C., Thomas P. A., White S. D. M., 2020, *MNRAS*, 491, 5795
- Hirschmann M., Naab T., Somerville R. S., Burkert A., Oser L., 2012, *MNRAS*, 419, 3200
- Hopkins P. F., Hernquist L., Cox T. J., Robertson B., Di Matteo T., Springel V., 2006, *ApJ*, 639, 700
- Hopkins P. F., Cox T. J., Younger J. D., Hernquist L., 2009, *ApJ*, 691, 1168
- Hunter J. D., 2007, *Computing in Science & Engineering*, 9, 90
- Hutter A., Dayal P., LeGrand L., Gottlöber S., Yepes G., 2021, *MNRAS*, 506, 215
- Izquierdo-Villalba D., Bonoli S., Dotti M., Sesana A., Rosas-Guevara Y., Spinoso D., 2020, *MNRAS*, 495, 4681
- Jespersen C. K., Steinhardt C. L., Somerville R. S., Lovell C. C., 2025, *ApJ*, 982, 23
- Jiang L., Helly J. C., Cole S., Frenk C. S., 2014, *MNRAS*, 440, 2115
- Kauffmann G., 1996, *MNRAS*, 281, 487
- Kauffmann G., Haehnelt M., 2000, *MNRAS*, 311, 576
- Kennicutt Jr. R. C., 1983, *ApJ*, 272, 54
- Kennicutt Jr. R. C., 1989, *ApJ*, 344, 685
- Kennicutt Jr. R. C., 1998, *ARA&A*, 36, 189
- Kennicutt R. C., Evans N. J., 2012, *ARA&A*, 50, 531
- Krumholz M. R., McKee C. F., Tumlinson J., 2009, *ApJ*, 693, 216
- Lacey C. G., et al., 2016, *MNRAS*, 462, 3854
- Lagos C. D. P., Lacey C. G., Baugh C. M., Bower R. G., Benson A. J., 2011, *MNRAS*, 416, 1566
- Lagos C. d. P., Lacey C. G., Baugh C. M., 2013, *MNRAS*, 436, 1787
- Lagos C. d. P., Tobar R. J., Robotham A. S. G., Obreschkow D., Mitchell P. D., Power C., Elahi P. J., 2018, *MNRAS*, 481, 3573
- Lagos C. d. P., et al., 2024, *MNRAS*, 531, 3551
- Lagos C. d. P., et al., 2025, *MNRAS*, 536, 2324
- Lee J., et al., 2014, *MNRAS*, 445, 4197
- Leung G. C. K., et al., 2023, *ApJ*, 954, L46
- Lovell C. C., Thomas P. A., Wilkins S. M., 2018, *MNRAS*, 474, 4612
- Lovell C. C., Vijayan A. P., Thomas P. A., Wilkins S. M., Barnes D. J., Irodotou D., Roper W., 2021, *MNRAS*, 500, 2127
- Lovell C. C., Harrison I., Harikane Y., Tacchella S., Wilkins S. M., 2023a, *MNRAS*, 518, 2511
- Lovell C. C., et al., 2023b, *MNRAS*, 525, 5520
- Lu Y., et al., 2014, *ApJ*, 795, 123
- Lu S., Frenk C. S., Bose S., Lacey C. G., Cole S., Baugh C. M., Helly J. C., 2025, *MNRAS*, 536, 1018
- Malbon R. K., Baugh C. M., Frenk C. S., Lacey C. G., 2007, *MNRAS*, 382, 1394
- Maraston C., 2005, *MNRAS*, 362, 799
- Matthee J., et al., 2024, *ApJ*, 963, 129
- McCarthy I. G., Frenk C. S., Font A. S., Lacey C. G., Bower R. G., Mitchell N. L., Balogh M. L., Theuns T., 2008, *MNRAS*, 383, 593
- McKee C. F., Krumholz M. R., 2010, *ApJ*, 709, 308
- Meier D. L., 2002, *New Astronomy Reviews*, 46, 247
- Merlin E., Chiosi C., Piovani L., Grassi T., Buonomo U., La Barbera F., 2012, *MNRAS*, 427, 1530
- Mitchell P. D., et al., 2018, *MNRAS*, 474, 492
- Mitchell P. D., Schaye J., Bower R. G., Crain R. A., 2020, *MNRAS*, 494, 3971
- Monaco P., Benson A. J., De Lucia G., Fontanot F., Borgani S., Boylan-Kolchin M., 2014, *MNRAS*, 441, 2058
- Mutch S. J., Geil P. M., Poole G. B., Angel P. W., Duffy A. R., Mesinger A., Wyithe J. S. B., 2016, *MNRAS*, 462, 250
- Narayanan D., et al., 2024, *ApJ*, 961, 73
- Navarro-Carrera R., Rinaldi P., Caputi K. I., Iani E., Kokorev V., van Mierlo S. E., 2024, *ApJ*, 961, 207
- Navarro J. F., Frenk C. S., White S. D. M., 1996, *ApJ*, 462, 563
- Nulsen P. E. J., Fabian A. C., 2000, *MNRAS*, 311, 346
- Overzier R. A., 2016, *A&ARv*, 24, 14
- Pacifici C., et al., 2016, *ApJ*, 832, 79
- Pandya V., et al., 2020, *ApJ*, 905, 4
- Planck Collaboration et al., 2014, *A&A*, 571, A1
- Popesso P., et al., 2023, *MNRAS*, 519, 1526
- Porter L. A., Somerville R. S., Primack J. R., Johansson P. H., 2014, *MNRAS*, 444, 942
- Poulton R. J. J., Power C., Robotham A. S. G., Elahi P. J., Lagos C. D. P., 2021, *MNRAS*, 501, 2810
- Roberts-Borsani G., et al., 2024, *ApJ*, 976, 193
- Robertson B., Cox T. J., Hernquist L., Franx M., Hopkins P. F., Martini P., Springel V., 2006, *ApJ*, 641, 21
- Robertson B., et al., 2024, *ApJ*, 970, 31
- Rodriguez-Gomez V., et al., 2015, *MNRAS*, 449, 49
- Roper W. J., Thomas P. A., Srisawat C., 2020, *MNRAS*, 494, 4509
- Russell T. A., et al., 2024, *arXiv e-prints*, p. [arXiv:2412.11861](https://arxiv.org/abs/2412.11861)
- Saghiha H., Simon P., Schneider P., Hilbert S., 2017, *A&A*, 601, A98
- Salpeter E. E., 1955, *ApJ*, 121, 161
- Schaye J., 2004, *ApJ*, 609, 667
- Schaye J., Dalla Vecchia C., 2008, *MNRAS*, 383, 1210
- Schaye J., et al., 2015, *MNRAS*, 446, 521
- Schaye J., et al., 2025, *arXiv e-prints*, p. [arXiv:2508.21126](https://arxiv.org/abs/2508.21126)
- Shakura N. I., Sunyaev R. A., 1973, *A&A*, 24, 337
- Silva L., Granato G. L., Bressan A., Danese L., 1998, *ApJ*, 509, 103
- Simha V., Cole S., 2017, *MNRAS*, 472, 1392
- Simpson C. M., Grand R. J. J., Gómez F. A., Marinacci F., Pakmor R., Springel V., Campbell D. J. R., Frenk C. S., 2018, *MNRAS*, 478, 548
- Somerville R. S., Davé R., 2015, *ARA&A*, 53, 51

Somerville R. S., Kolatt T. S., 1999, *MNRAS*, **305**, 1

Somerville R. S., Primack J. R., Faber S. M., 2001, *MNRAS*, **320**, 504

Somerville R. S., Hopkins P. F., Cox T. J., Robertson B. E., Hernquist L., 2008, *MNRAS*, **391**, 481

Somerville R. S., Popping G., Trager S. C., 2015, *MNRAS*, **453**, 4337

Somerville R. S., Yung L. Y. A., Lancaster L., Menon S., Sommovigo L., Finkelstein S. L., 2025, *arXiv e-prints*, p. [arXiv:2505.05442](https://arxiv.org/abs/2505.05442)

Springel V., White S. D. M., Tormen G., Kauffmann G., 2001, *MNRAS*, **328**, 726

Springel V., et al., 2005, *Nature*, **435**, 629

Springel V., Pakmor R., Zier O., Reinecke M., 2021, *MNRAS*, **506**, 2871

Steinhardt C. L., Kokorev V., Rusakov V., Garcia E., Sneppen A., 2023, *ApJ*, **951**, L40

Stevens A. R. H., Croton D. J., Mutch S. J., 2016, *MNRAS*, **461**, 859

Stevens A. R. H., Sinha M., Rohl A., Sammons M. W., Hadzhiyska B., Hernández-Aguayo C., Hernquist L., 2024, *Publ. Astron. Soc. Australia*, **41**, e053

Suess K. A., et al., 2022, *ApJ*, **935**, 146

Sun G., Faucher-Giguère C.-A., Hayward C. C., Shen X., Wetzel A., Cochrane R. K., 2023, *ApJ*, **955**, L35

Sutherland R. S., Dopita M. A., 1993, *ApJS*, **88**, 253

Taylor A. J., et al., 2024, *arXiv e-prints*, p. [arXiv:2409.06772](https://arxiv.org/abs/2409.06772)

Thomas P. A., Lovell C. C., Maltz M. G. A., Vijayan A. P., Wilkins S. M., Irodotou D., Roper W. J., Seeyave L., 2023, *MNRAS*, **524**, 43

Trussler J., Maiolino R., Maraston C., Peng Y., Thomas D., Goddard D., Lian J., 2020, *MNRAS*, **491**, 5406

Trussler J. A. A., et al., 2024, *MNRAS*, **527**, 11627

Turner J. C., Roper W. J., Vijayan A. P., Newman S. L., Wilkins S. M., Lovell C. C., Liao S., Seeyave L. T. C., 2025, *arXiv e-prints*, p. [arXiv:2509.16111](https://arxiv.org/abs/2509.16111)

Valentino F., et al., 2023, *ApJ*, **947**, 20

Vani A., Ayromlou M., Kauffmann G., Springel V., 2025, *MNRAS*, **536**, 777

Vijayan A. P., Lovell C. C., Wilkins S. M., Thomas P. A., Barnes D. J., Irodotou D., Kuusisto J., Roper W. J., 2021, *MNRAS*, **501**, 3289

Visser-Zadvornyi A. I., Carstairs M. E., Oman K. A., Verheijen M. A. W., 2025, *arXiv e-prints*, p. [arXiv:2503.15183](https://arxiv.org/abs/2503.15183)

Weaver J. R., et al., 2023, *A&A*, **677**, A184

Weibel A., et al., 2024a, *arXiv e-prints*, p. [arXiv:2409.03829](https://arxiv.org/abs/2409.03829)

Weibel A., et al., 2024b, *MNRAS*, **533**, 1808

White S. D. M., Frenk C. S., 1991, *ApJ*, **379**, 52

Whitler L., et al., 2025, *ApJ*, **992**, 63

Wiersma R. P. C., Schaye J., Smith B. D., 2009a, *MNRAS*, **393**, 99

Wiersma R. P. C., Schaye J., Theuns T., Dalla Vecchia C., Tornatore L., 2009b, *MNRAS*, **399**, 574

Xiao M., et al., 2024, *Nature*, **635**, 311

Xu K., et al., 2025, *arXiv e-prints*, p. [arXiv:2503.21724](https://arxiv.org/abs/2503.21724)

Yates R. M., Henriques B. M. B., Fu J., Kauffmann G., Thomas P. A., Guo Q., White S. D. M., Schady P., 2021a, *MNRAS*, **503**, 4474

Yates R. M., Péroux C., Nelson D., 2021b, *MNRAS*, **508**, 3535

Yates R. M., Hendriks D., Vijayan A. P., Izzard R. G., Thomas P. A., Das P., 2024, *MNRAS*, **527**, 6292

Yung L. Y. A., Somerville R. S., Finkelstein S. L., Popping G., Davé R., 2019a, *MNRAS*, **483**, 2983

Yung L. Y. A., Somerville R. S., Popping G., Finkelstein S. L., Ferguson H. C., Davé R., 2019b, *MNRAS*, **490**, 2855

Yung L. Y. A., Somerville R. S., Popping G., Finkelstein S. L., 2020, *MNRAS*, **494**, 1002

Yung L. Y. A., Somerville R. S., Finkelstein S. L., Hirschmann M., Davé R., Popping G., Gardner J. P., Venkatesan A., 2021, *MNRAS*, **508**, 2706

Yung L. Y. A., et al., 2022, *MNRAS*, **515**, 5416

Yung L. Y. A., Somerville R. S., Finkelstein S. L., Wilkins S. M., Gardner J. P., 2024a, *MNRAS*, **527**, 5929

Yung L. Y. A., Somerville R. S., Nguyen T., Behroozi P., Modi C., Gardner J. P., 2024b, *MNRAS*, **530**, 4868

Zhang Y., et al., 2025, *arXiv e-prints*, p. [arXiv:2508.08577](https://arxiv.org/abs/2508.08577)

van de Voort F., Bahé Y. M., Bower R. G., Correa C. A., Crain R. A., Schaye J., Theuns T., 2017, *MNRAS*, **466**, 3460

## APPENDIX A: PHYSICAL PROPERTIES

The top row of Figure A1 shows the SMF obtained after convolving stellar masses with errors drawn from a Gaussian distribution of width of 0.3 dex. By invoking a relatively small error, we find that the predictions by L-GALAXIES are within range of observations.

The bottom row of Figure A1 shows the SFS predicted by the models. The slope of the SFS is fairly similar across models. At  $z = 5$ , L-GALAXIES and SC-SAM exhibit a slightly steeper slope, with a median  $\sim 0.5$  dex lower than that of GALFORM and SHARK at the lowest stellar masses ( $M_{\star} = 10^{7.5} M_{\odot}$ ). At higher stellar masses ( $M_{\star} > 10^9 M_{\odot}$ ), the models converge. We also show the best-fitting relation provided by Popesso et al. (2023), who convert measurements of the SFS from 50 studies, published between 2007 and 2022, to a Kennicutt & Evans (2012) calibration. We also show a linear fit provided by Roberts-Borsani et al. (2024) to the data of 330 spectroscopically-confirmed galaxies between  $5 < z < 7$ . SFRs are estimated from UV luminosity by applying a Kennicutt (1998) conversion. The models generally show good agreement with the SFS measured by Popesso et al. (2023). The gradient of the SFS measured by Roberts-Borsani et al. (2024) is gentler, and favours the higher SFRs at low stellar masses ( $M_{\star} \sim 10^8 M_{\odot}$ ) that are observed in GALFORM and SHARK. At  $M_{\star} > 10^9 M_{\odot}$ , the models predict that galaxies are more highly star-forming than estimated by Roberts-Borsani et al. (2024). Finally, we also plot measurements by Clarke et al. (2024) for individual galaxies, using SFRs derived from the  $H\alpha$  luminosity, which is sensitive to star formation on short timescales ( $\sim 5$  Myr).

## APPENDIX B: CONVERGENCE TESTS

In §3.2.2, we described the convergence tests performed to determine an appropriate DMO resolution for our analysis. The main findings for each SAM are summarised as follows:

- **GALFORM:** Overall, we find that the model makes very similar predictions when run on simulations with particle masses in the range  $M_{\text{DM}} = 8.36 \times 10^7 - 3.22 \times 10^8 M_{\odot}$ . At the highest redshifts ( $z \geq 10.5$ ), the highest resolution ( $M_{\text{DM}} = 1.15 \times 10^7 M_{\odot}$ ) run produces a lower SMF and SFRF than the benchmark run, by  $\sim 0.5$  dex. Additionally, across all redshifts, the highest resolution run predicts a  $\sim 0.5 - 2$  dex excess of black holes at  $M_{\text{BH}} < 10^{6.5} M_{\odot}$ , and a lower stellar-to-black hole mass ratio in the same black hole mass range, compared to the benchmark resolution run.

- **L-GALAXIES:** We generally find good convergence across the tested resolution range for the quantities shown, with results in agreement with predictions from the Yates et al. (2024) model when run on the complete set of MILLENNIUM-II trees, and predictions from Henriques et al. (2020) when run on the complete set of MILLENNIUM-I trees. An exception to this is the BHMF, where the result of the highest resolution ( $M_{\text{DM}} = 1.15 \times 10^7 M_{\odot}$ ) run is  $\sim 1$  dex lower than that of the lowest resolution run ( $M_{\text{DM}} = 3.22 \times 10^8 M_{\odot}$ ). The BHMF appears to increase with increasing particle mass. It is unclear as to whether the result converges at particle masses beyond the tested range. Consequently, the stellar-to-black hole mass relation is also resolution-dependent – at a given stellar mass, we find a  $\sim 1 - 1.5$  dex difference between the SMBH masses predicted by the highest and lowest resolutions.

- **SC-SAM:** We find good convergence across all resolutions, and good agreement with predictions by Yung et al. (2024a), except when it comes to black hole properties. Interestingly, the resolution-dependence of the BHMF is the reverse of that observed

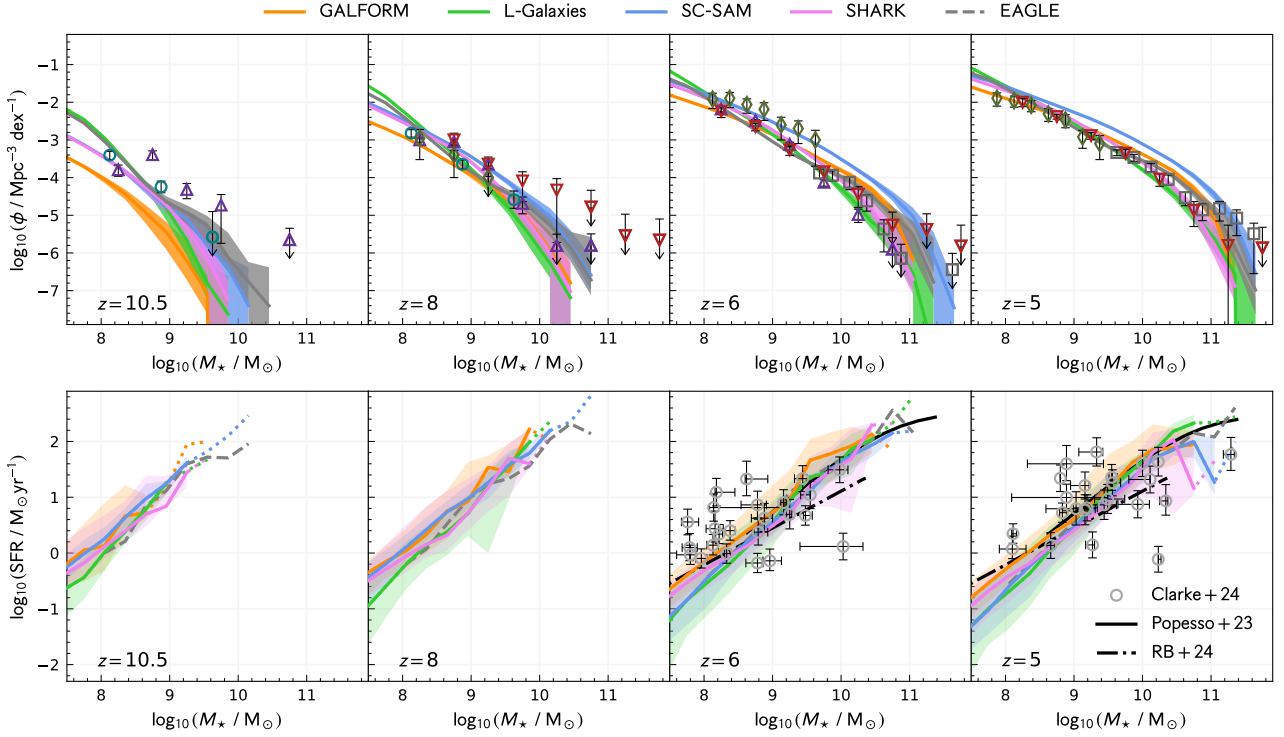


**Figure A1.** Top row: SMF predicted by the models across a range of redshifts, obtained after convolving stellar masses with errors drawn from a Gaussian distribution of width of 0.3 dex. Shaded regions denote the  $1\sigma$  range for 500 iterations of errors. Observations are shown as scatter points (please see Figure 2 for the legend). Bottom row: Star formation rate as a function of stellar mass, predicted by the models across a range of redshifts. Note that a stellar mass cut of  $M_* > 10^8 M_\odot$  is applied to the EAGLE results, and that the EAGLE predictions at  $z = 10.5$  are in fact at  $z = 10$ , as outputs of the fiducial FLARES suite are saved at integer redshift. For the SAMs, dotted lines denote bins containing fewer than 10 galaxies. Observational measurements by Popesso et al. (2023) and Roberts-Borsani et al. (2024) are plotted as solid and dot-dashed black lines respectively, and measurements by Clarke et al. (2024) are plotted as scatter points.

in L-GALAXIES – at  $M_{\text{BH}} < 10^6 M_\odot$ , we find that the higher the resolution, the higher the BHMF. The BHMFs appear to converge at  $M_{\text{BH}} > 10^6 M_\odot$ , especially at lower redshifts ( $z = 5 - 6$ ). The stellar-to-black hole mass relation also changes with particle mass. At  $M_{\text{BH}} < 10^6 M_\odot$ , we find that the lower the particle mass, the smaller the stellar-to-black hole mass ratio. At  $M_{\text{BH}} > 10^6 M_\odot$ , there is better convergence between the different resolutions.

- **SHARK:** We find that the model predictions generally converge for particle masses in the range  $M_{\text{DM}} = 8.36 \times 10^7 - 3.22 \times 10^8 M_\odot$ . The highest resolution ( $M_{\text{DM}} = 1.15 \times 10^7 M_\odot$ ) run predicts a SMF and SFRF  $\sim 0.3 - 0.5$  dex lower than the benchmark run. This difference shows up in the SHMR as well, where for a given halo mass, this run tends to produce galaxies with a lower stellar mass, particularly around the characteristic turnover at  $M_{\text{halo}} \sim 10^{11.5} M_\odot$ . Additionally, the  $M_{\text{DM}} = 1.15 \times 10^7 M_\odot$  run predicts a lower BHMF than the benchmark run. As the stellar-to-black hole mass relation is converged across the range of particle masses tested this difference in the BHMF can be attributed to the aforementioned differences in the SMF.

### APPENDIX C: PASSIVE SATELLITES IN SAMs

Figure C1 shows, for each SAM, how the sSFR, cold gas mass and galaxy type evolves with time, for a handful of passive satellite galaxies. Centrals are labelled as type 0. In SC-SAM, type 1 galaxies are satellites of centrals, while type 2 galaxies are satellites of satellites. In the remaining SAMs, type 1 galaxies are satellites associated with

a resolved subhalo, while type 2 satellites are those whose associated subhalo have become sub-resolution. In Figure C1, the time axis is adjusted such that the galaxies transition from a central to satellite at  $t = 0$ . Generally, the sSFR of a galaxy tends to trace its cold gas mass. GALFORM and SC-SAM show a steady decline in the cold gas mass and hence sSFR after a galaxy becomes a satellite. In SHARK, the cold gas mass evolves more erratically, dropping sharply in some galaxies while declining more steadily in others. As for L-GALAXIES, the cold gas mass is observed to decline after a galaxy becomes a satellite, however, the resultant change in the sSFR is not as obvious, perhaps due to the lower snapshot cadence adopted.

This paper has been typeset from a  $\text{\TeX}/\text{\LaTeX}$  file prepared by the author.

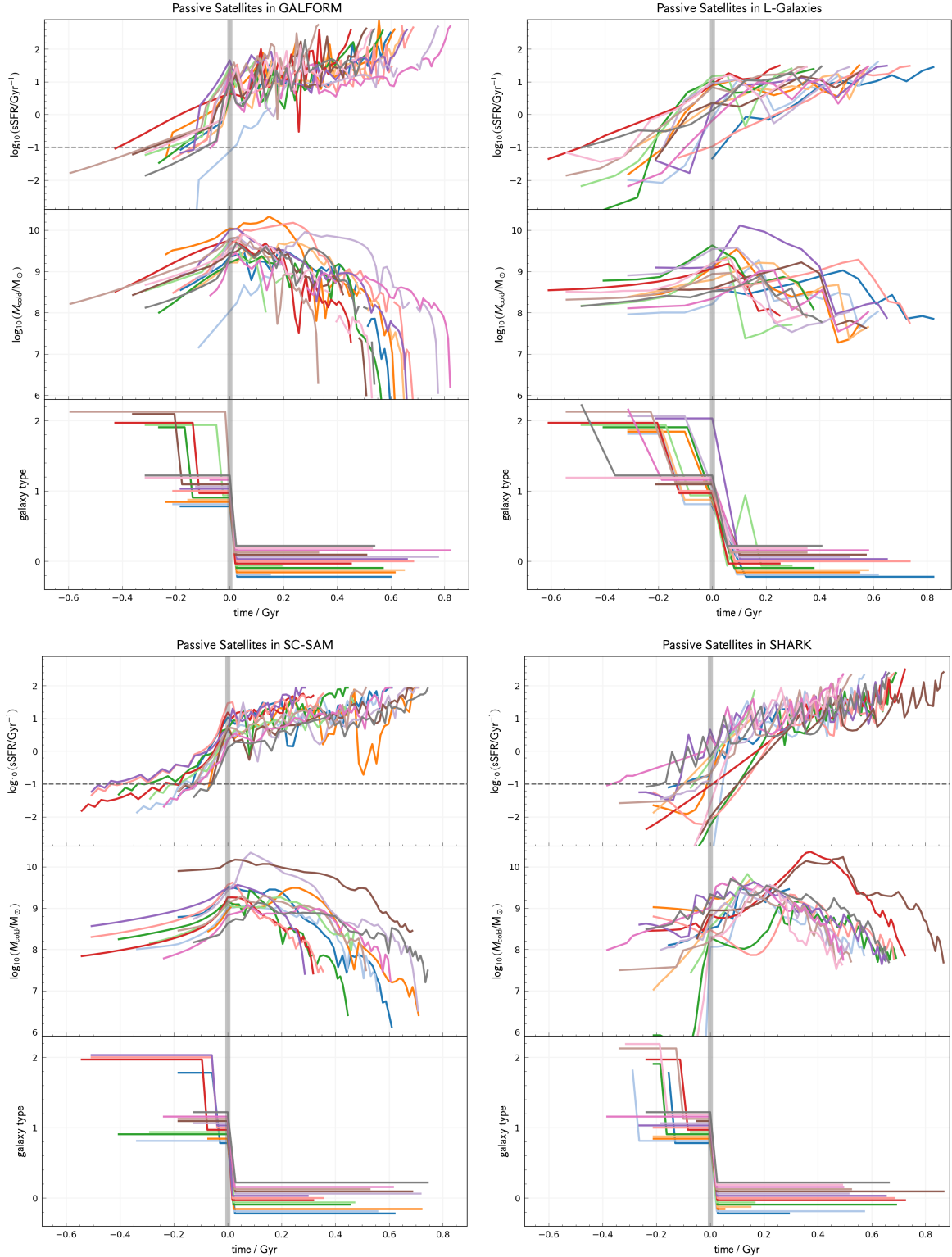


**Figure C1.** Each plot shows, for a particular SAM, the evolutionary histories of 15 randomly chosen passive satellites with  $\log_{10}(M_{\star}/M_{\odot}) > 9$ . The panels within each plot show, from top to bottom, the sSFR, cold gas mass and galaxy type of each galaxy as a function of time (see text for explanation of types). The dashed horizontal line in the top panel represents the sSFR threshold below which a galaxy is considered passive. Note that the galaxy type of each galaxy is slightly offset for clarity. The galaxies are chosen at  $z = 5$ , but aligned such that the transition from central to satellite occurs at  $t = 0$ , marked by the grey vertical line. The x-axis thus shows the time to the transition occurring, with time moving from right to left.